

# AnatomiX, an Anatomy-Aware Grounded Multimodal Large Language Model for Chest X-Ray Interpretation

Anees Ur Rehman Hashmi  
Hasso Plattner Institute  
Potsdam, Germany  
anees.hashmi@hpi.de

Numan Saeed  
MBZUAI  
Abu Dhabi, UAE  
numan.saeed@mbzuai.ac.ae

Christoph Lippert  
Hasso Plattner Institute  
Potsdam, Germany  
christoph.lippert@hpi.de

## Abstract

*Multimodal medical large language models have shown substantial progress in chest X-ray interpretation but continue to face challenges in spatial reasoning and anatomical understanding. Although existing grounding techniques improve overall performance, they often fail to establish a true anatomical correspondence, resulting in incorrect anatomical understanding in the medical domain. To address this gap, we introduce AnatomiX, a multitask multimodal large language model for anatomically grounded chest X-ray interpretation. Inspired by the radiological workflow, AnatomiX adopts a two stage approach: first, it identifies anatomical structures and extracts their features, and then leverages a large language model to perform diverse downstream tasks such as phrase grounding, report generation, visual question answering, and image understanding. Extensive experiments across multiple benchmarks demonstrate that AnatomiX achieves superior anatomical reasoning and delivers over 25% improvement in performance on anatomy grounding, phrase grounding, grounded diagnosis and grounded captioning tasks compared to existing approaches. Code and pretrained model are available at [aneesurhashmi.github.io/anatomix](https://aneesurhashmi.github.io/anatomix).*

## 1. Introduction

Multimodal Large Language Models (MLLMs) are being increasingly applied in the natural and medical imaging domain to perform multiple tasks using a single model [36]. These models typically consist of an image encoder and a Large Language Model (LLM), and utilize the pretrained LLM’s strengths by passing image embeddings along with a text prompt into the LLM to perform downstream tasks [21]. The pretrained LLMs are generally trained on very large text corpora and therefore demonstrate strong text generation capabilities, making them suitable for a diverse set of downstream tasks after supervised fine-tuning and

instruction tuning [1, 25]. However, owing partly to their autoregressive design and the challenges of merging vision and language modalities, MLLMs still struggle with fine-grained spatial understanding, for instance, when reasoning about positions of multiple objects or their relative spatial relations in a scene [22, 34].

This issue of MLLMs has previously been addressed by introducing object grounding, which aligns the text concepts with the objects in the image [29, 33]. Grounding in MLLMs is usually achieved by training the model on a dataset containing the names or descriptions of local objects in the image plus their bounding boxes or segmentation masks as spatial markers. This in turn improves the reasoning abilities of MLLMs with better concept understanding, making them applicable in the medical domain, where spatial reasoning is essential. In particular, chest X-ray (CXR) interpretation greatly benefits from such multimodal reasoning, as accurate localization and semantic alignment between textual findings and radiographic regions are crucial for diagnosis. MLLMs like ViviMed [24], ChexAgent [7], RadVLM [10] and MAIRA-2 [4] show that grounding via special tokens yields consistent performance gains on CXR image tasks.

Although incorporating grounding through additional tokens has improved MLLMs’ spatial reasoning, it remains insufficient for the fine-grained localization and differentiation required in medical imaging, where anatomically distinct regions often exhibit highly similar visual textures and appearances [34]. As illustrated in Fig. 1, current state-of-the-art (SOTA) MLLM fails to correctly localize lesions or identify the correct anatomical objects when presented with flipped images - where the left and right sides are switched. These models may perform well on standard orientations but fail when spatial cues are inverted, revealing that they overly rely on spatial correlations rather than recognition of anatomical structures, exposing a critical gap between visual grounding and medical comprehension.

This weak anatomical understanding in current medical MLLMs is likely due to their single-step visual grounding

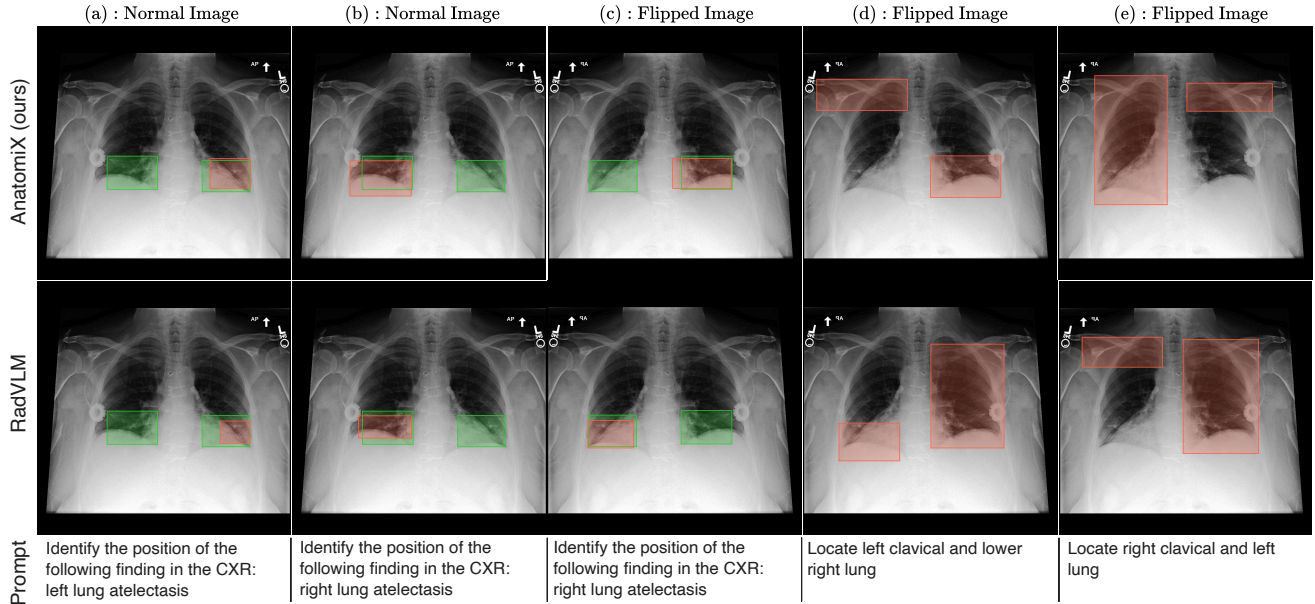


Figure 1. Comparison between AnatomicX and RadVLM [10] in anatomy understanding. (a) and (b) show both models predicting the disease on the correct side (color scheme: red for model’s output, green for all ground truth locations). (c), (d) and (e) show models’ outputs for the same image flipped on the vertical axis (left  $\leftrightarrow$  right), where RadVLM completely fails to recognize the correct anatomical object, while AnatomicX successfully recognizes the correct anatomies, showcasing high anatomical understanding

process. Specifically, these models must implicitly detect the correct anatomical objects within an image before performing the downstream task. This one-step process differs fundamentally from the workflow of radiologists, who iteratively identify, localize, and evaluate each anatomical structure before drawing diagnostic conclusions. To address this issue, we introduce *AnatomicX*, an anatomy-aware grounded MLLM for chest X-Ray interpretation. AnatomicX uses a two stage process to first identify different thoracic anatomical objects (organs) before performing the task; thereby, showing a high anatomical understanding compared to existing CXR grounding MLLMs as shown in Fig. 1. Our proposed model significantly outperforms SOTA models on four grounding tasks and shows SOTA or on-par performance on report generation, VQA and image understanding tasks. Extensive experiments on a large collection of datasets show the high reasoning and anatomical understanding capabilities of AnatomicX. In summary, our work makes the following contributions:

- We introduce *AnatomicX*, an anatomy-aware grounded multimodal large language model for CXR interpretation.
- AnatomicX improves anatomical understanding by achieving SOTA performance on diverse grounding tasks, while maintaining on-par or better performance on report-generation, VQA and image understanding tasks.
- We demonstrate the robustness of AnatomicX across different datasets and challenging settings, and validate the contribution of each component in ablation experiments.

## 2. Related Work

Early adaptations of MLLMs to radiology primarily involve fine-tuning general-domain models on medical datasets. LLaVA-Med [17] and RadVLM [10] extend LLaVA [21] for multi-task CXR benchmarks, improving both report generation and VQA. Several works introduce explicit grounding for CXR tasks: ViviMed [24] and MedRG [38] pair the Segment-Anything model [15] with an LLM for detection and segmentation, while MAIRA-2 [4] enables grounded report generation through additional tokens. Similarly, RadVLM [10] constructs a large instruction dataset for diverse CXR tasks, whereas CheXagent [7] applies contrastive learning and instruction tuning to enhance phrase grounding and CXR report generation. Radialog [28] supports multi-turn CXR conversations, and MedGemma [31] adapts Gemma-3 for general purpose medical tasks by fine-tuning on large-scale medical datasets. More recently, AOR [18] introduced region level information in LLM for CXR interpretation; however, this model is not yet publicly available for testing and comparison.

Most prior efforts adapt general-domain MLLMs rather than developing domain-specific architectures. CheX [26] advances toward anatomy-aware modeling by incorporating anatomical objects from CXR reports but lacks prompt-based interaction and generative flexibility. Overall, existing CXR MLLMs rely on instruction tuning and large-scale radiology datasets, achieving strong benchmark per-

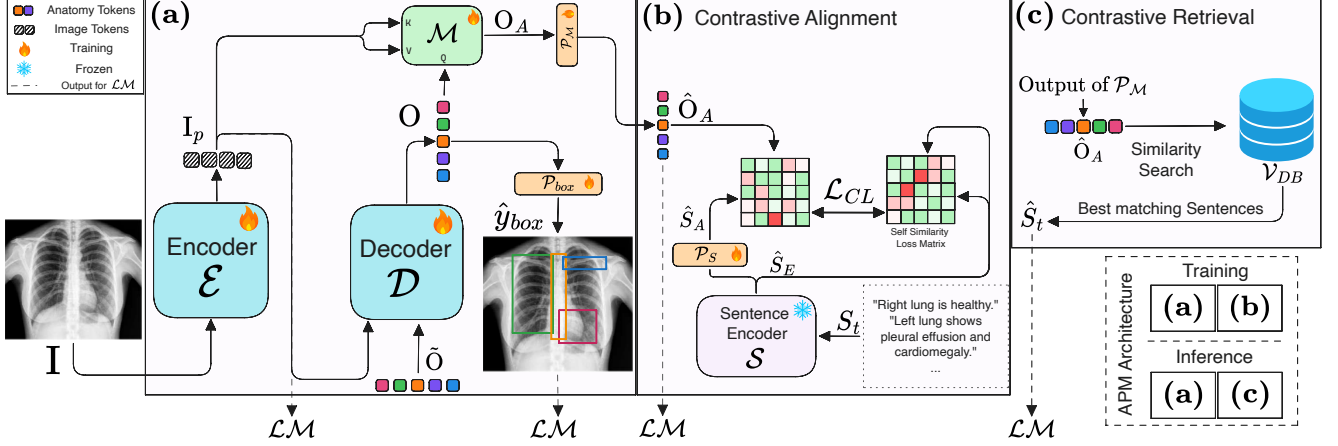


Figure 2. Anatomy Perception Module (APM) architecture (a): The encoder  $\mathcal{E}$  outputs image embedding  $I_p$ , while the decoder  $\mathcal{D}$  and feature extraction module  $\mathcal{M}$  output object bounding boxes  $\hat{y}_{box}$ , and anatomical object tokens  $\hat{O}_A$ , respectively. Different colors in  $\hat{O}$ ,  $O$  and  $\hat{O}_A$  represent specific anatomical objects. (b) shows the contrastive alignment using frozen sentence encoder  $\mathcal{S}$  and self-similarity loss. (c): The vector database ( $\mathcal{V}_{DB}$ ) contains the text sentences and embeddings used for contrastive retrieval. (Bottom right): APM uses (a) and (b) during training, and replaces (b) with (c) during inference. The  $\mathcal{P}$  represent different FC projectors described in section 3.1.

formance yet showing limited reasoning and anatomical understanding [34]. In contrast, our approach introduces a two-stage anatomy-aware pipeline that explicitly models thoracic structures before performing downstream tasks.

### 3. Methodology

This section describes the architecture of AnATOMiX, which comprises two primary components: The Anatomy Perception Module and a large language model outlined below.

#### 3.1. Anatomy Perception Module

Given an input CXR image  $I$ , the objective of the Anatomy Perception Module (APM) is to extract a global image representation along with fine-grained features corresponding to  $N$  thoracic anatomical objects. The resulting representations are subsequently used by an LLM for downstream tasks. The APM adopts a multi-task learning framework that jointly learns global image features, object localization through bounding boxes, and their detailed anatomical representations, while also retrieving textual descriptions associated with each anatomical object. Fig. 2 shows the detailed architecture of the APM, which consists of an image encoder ( $\mathcal{E}$ ), a decoder ( $\mathcal{D}$ ), a feature extraction module ( $\mathcal{M}$ ) and a sentence encoder ( $\mathcal{S}$ ). The details of each component are given below.

##### Image Encoder $\mathcal{E}$ and Decoder $\mathcal{D}$ :

The input image  $I$  is first encoded by the image encoder  $\mathcal{E}$  producing the image representation  $I_p \in \mathbb{R}^{P \times d}$  which consists of  $P$  patch embedding vectors of dimension  $d$ . Together, these form a global representation of the image. These embeddings serve as the shared representation of vi-

sual information for subsequent modules. Specifically,  $I_p$  is provided both to the feature extractor  $\mathcal{M}$ , which focuses on semantic anatomy cues, and to the decoder  $\mathcal{D}$ , which is inspired by DETR [6]. The decoder processes  $I_p$  jointly with  $N$  learnable object tokens  $\tilde{O} = [\tilde{o}^1, \dots, \tilde{o}^N]$ , using transformer blocks to perform cross-attention between tokens and image patches. Through this interaction, each object token learns to attend to relevant anatomical regions, resulting in updated token embeddings  $O$  that encode the localization of the  $N$  anatomical objects.

$$O = \mathcal{D}(I_p, \tilde{O}) \quad (1)$$

where  $O \in \mathbb{R}^{N \times d} = [o^1, \dots, o^N; o^i \in \mathbb{R}^d]$

The object tokens  $O$  are projected using a fully connected (FC) projector  $\mathcal{P}_{box}$  to predict a bounding box for each anatomical object ( $\hat{y}_{box} = \mathcal{P}_{box}(O)$ ), as illustrated in Fig. 2. Unlike DETR [6],  $O$  is not permutation invariant, which means that each element of  $O$  corresponds to exactly one predefined anatomical object. This design enables each token  $o^i$  to focus on and extract information related to the  $i^{th}$  anatomical object from  $I_p$ . To effectively learn the  $\hat{y}_{box}$  localization, we use a combination of L1 and intersection over union (IoU) losses as shown in eq. 2 and 3.

$$\mathcal{L}_{IoU}(\hat{y}_{box}, y_{box}) = 1 - \frac{|\hat{y}_{box} \cap y_{box}|}{|\hat{y}_{box} \cup y_{box}|} \quad (2)$$

$$\mathcal{L}_{box} = \lambda_1 (|\hat{y}_{box} - y_{box}|) + \lambda_2 \mathcal{L}_{IoU}(\hat{y}_{box}, y_{box}) \quad (3)$$

where  $y_{box}$  represents ground truth bounded boxes,  $\lambda_1 = 5$  and  $\lambda_2 = 2$  are the weightings of the L1 Loss and the  $\mathcal{L}_{IoU}$

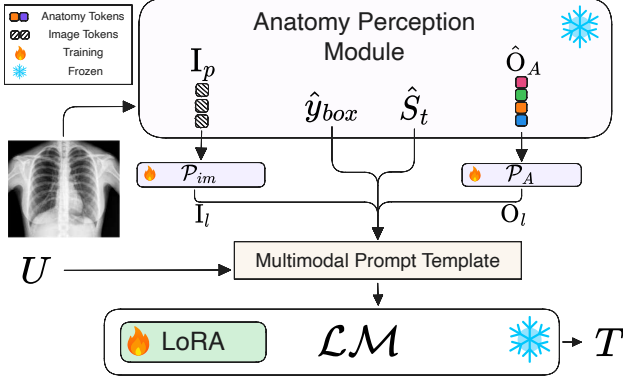


Figure 3. Overall architecture of AnATOMiX. The outputs of the APM and the user prompt  $U$  are added to a structured multimodal prompt template before being passed to the  $\mathcal{LM}$ , which generates the response  $T$ .  $\mathcal{P}_{im}$  and  $\mathcal{P}_A$  represent FC projectors as described in section 3.2.

Loss, respectively, set to the default values used in DETR.

### Feature Extraction Module $\mathcal{M}$ :

In addition to predictions of the bounding boxes in the decoder output, we leverage the spatial information encoded in  $O$  to extract fine-grained representations of each anatomical object through the feature extraction module  $\mathcal{M}$ . Within  $\mathcal{M}$ , cross-attention is computed between  $O$  and image patches  $I_p$  as shown in eq. 4, where the anatomical object tokens  $O$  serve as queries ( $Q$ ), and the image embedding  $I_p$  provides the keys ( $K$ ) and values ( $V$ ). Conceptually,  $\mathcal{M}$  can be viewed as an extension of the decoder  $\mathcal{D}$ , where the image representation  $I_p$  is re-included via a skip connection.

$$O_A = \mathcal{M}(Q, K, V) = \text{Softmax} \left( \frac{QK^T}{\sqrt{d}} \right) V \quad (4)$$

where  $Q = OW_Q$  is the query matrix,  $K = I_pW_K$  is the key matrix and  $V = I_pW_V$  is the value matrix.

The output  $O_A$  represent localized features for the anatomical objects at the corresponding positions specified by the predicted bounding boxes  $\hat{y}_{box}$  (see supp. Fig. A5). Subsequently, these features are projected to a lower-dimensional space ( $d \rightarrow s$ ) using the projection module  $\mathcal{P}_M$  as:  $\hat{O}_A = \mathcal{P}_M(O_A)$ , where  $\hat{O}_A \in \mathbb{R}^{N \times s}$ .

### Contrastive Alignment with $S$ :

During APM training, we perform localized contrastive alignment (Fig. 2-b) between each anatomical feature token  $\hat{o}_A^i \in \hat{O}_A$  and its corresponding textual description  $s^i \in S_t$ , where  $s^i$  specifies the radiological findings in the associated anatomical region (e.g. *Right Lung shows*

*pneumonia, pleural effusion and atelectasis.*). Since  $\hat{O}_A$  encodes fine-grained visual representations of  $N$  anatomical objects derived from the image embedding  $I_p$ , aligning these tokens with the corresponding text sentence embeddings enables the model to establish correspondences between visual and semantic representations. This alignment ensures that the visual tokens capture each anatomical region’s spatial and structural properties while linking them to clinically relevant textual concepts. The textual descriptions  $S_t$  are first encoded using the frozen sentence encoder  $\mathcal{S}$  (BiomedBERT [11]) to obtain embeddings  $\hat{S}_E \in \mathbb{R}^{N \times 768}$  as  $\hat{S}_E = \mathcal{S}(S_t)$ . Finally,  $\hat{S}_E$  is projected to a lower-dimensional space ( $768 \rightarrow s$ ) using a fully connected projector  $\mathcal{P}_S$  for efficient contrastive learning as  $\hat{S}_A = \mathcal{P}_S(\hat{S}_E)$ , where  $\hat{S}_A \in \mathbb{R}^{N \times s}$  represents projected text embeddings.

Radiological findings across thoracic anatomical objects often overlap or appear together, making it uncommon for an image to contain a finding in only one region. In such cases, using standard CLIP-style contrastive loss [30] can introduce many false negatives, as it assumes only one correct (positive) text–image pair per sample. To overcome this, we employ a soft contrastive loss that allows multiple degrees of similarity across anatomical regions. Specifically, we introduce a self-similarity matrix  $S_{self}$  (eq. 5), which permits non-zero similarity values for off-diagonal entries, reflecting the natural co-occurrence of anatomical observations (see the supp. material sec. S1 for details). We optimize this alignment using Kullback–Leibler (KL) divergence as shown in eq. 6, which measures distributional differences instead of enforcing discrete class boundaries [13]. This makes it well-suited for overlapping or correlated anatomical feature representations and preserving partial similarities among different anatomical objects’ features.

$$S_{self} = \hat{S}_E \hat{S}_E^T \quad (5)$$

$$\mathcal{L}_{CL}(\hat{S}_A, S_{self}) = \sum_i \hat{S}_A(i) \log \frac{\hat{S}_A(i)}{S_{self}(i)} \quad (6)$$

where  $S_{self} \in \mathbb{R}^{N \times N}$

Finally, we train APM end-to-end using a combination of bounding box prediction and contrastive alignment losses.

$$\mathcal{L}_{APM} = \mathcal{L}_{box} + \mathcal{L}_{CL} \quad (7)$$

### Contrastive Retrieval with $\mathcal{V}_{DB}$ :

Since the textual descriptions  $S_t$  associated with anatomical objects are available only during APM training, we replace the sentence encoder  $\mathcal{S}$  with a compact vector database  $\mathcal{V}_{DB}$  during inference as shown in Fig. 2-(c). This database stores all unique textual sentences corresponding to each

of the  $N$  anatomical regions, along with their precomputed embeddings. At inference time, each anatomical object token in  $\hat{O}_A$  is compared against the sentence embeddings in  $\mathcal{V}_{DB}$  to retrieve the most semantically similar sentence  $\hat{S}_t$  for that anatomical region as  $\hat{S}_t = \mathcal{V}_{DB}(\hat{O}_A)$ . The retrieved sentences are then passed to LLM, along with the anatomical object tokens  $\hat{O}_A$ , the predicted bounding boxes  $\hat{y}_{box}$ , and the image embeddings  $I_p$ . Additional implementation details of  $\mathcal{V}_{DB}$  are provided in the supp. material sec. S2.

### 3.2. Large Language Model

Given the outputs of APM — image embeddings  $I_p$ , predicted locations of  $N$  anatomical objects  $\hat{y}_{box}$  and their corresponding features  $\hat{O}_A$  and retrieved text descriptions  $\hat{S}_t$  - and the user prompt  $U$ , the large language model  $\mathcal{LM}$  generates a textual response  $T$  performing the task specified in  $U$ . To achieve this, we construct a multimodal prompt template (shown in supp. Fig. S2) that integrates the fine grained anatomical and textual information extracted in APM, and passes it to  $\mathcal{LM}$ . Fig. 3 shows the overall architecture of AnatomicX. Firstly, to align the embedding spaces of APM and  $\mathcal{LM}$ , we project both the image embedding  $I_p$  and anatomical object tokens embedding  $\hat{O}_A$  into  $\mathcal{LM}$ 's embedding space using FC projectors. Specifically,  $\mathcal{P}_{im} (d \rightarrow l)$  maps the image embedding to  $I_l = \mathcal{P}_{im}(I_p)$ , where  $I_l \in \mathbb{R}^{P \times l}$ , and  $\mathcal{P}_A (s \rightarrow l)$  maps the anatomical object token embedding to  $O_l = \mathcal{P}_A(\hat{O}_A)$ , where  $O_l \in \mathbb{R}^{N \times l}$ .

The language model  $\mathcal{LM}$  is based on MedGemma-4b-it [31] LLM architecture (excluding vision encoder). To enable anatomy aware reasoning, we extend the model's vocabulary by introducing  $N$  special tokens for anatomical objects ( $\langle obj\_i \rangle$  for  $i \in [0, N]$ ) and four additional tokens for spatial grounding ( $\langle box \rangle$ ,  $\langle /box \rangle$ ,  $\langle ref \rangle$ , and  $\langle /ref \rangle$ ). Each  $\langle obj\_i \rangle$  token corresponds to the feature representation of the  $i^{\text{th}}$  anatomical object,  $o_i^i$ , where  $O_l = [o_1^1, \dots, o_N^N]$ . By explicitly providing these object-specific tokens, the LLM can directly access the fine grained visual features of each anatomical object. This design allows  $\mathcal{LM}$  to directly reason over anatomical objects rather than implicitly inferring them from global image representations and then performing the task given in  $U$ . Finally, the  $\mathcal{LM}$  is trained for the next token prediction using Low-Rank Adaptation (LoRA) [12] and optimized with standard cross-entropy loss as shown in eq. 8.

$$\mathcal{L}_{\mathcal{LM}} = -\frac{1}{T} \sum_{t=1}^T \sum_{w \in V} y_t(w) \log p_{\mathcal{LM}}(w | x_{<t}) \quad (8)$$

$$p_{\mathcal{LM}}(w | x_{<t}) = \text{Softmax}(\mathcal{LM}(x_{<t})) \quad (9)$$

where  $T$  is the total number of tokens in the sequence,  $V$  is the vocabulary,  $x_{<t}$  represents the context tokens before position  $t$ ,  $y_t(w)$  is the one-hot ground truth distribution at

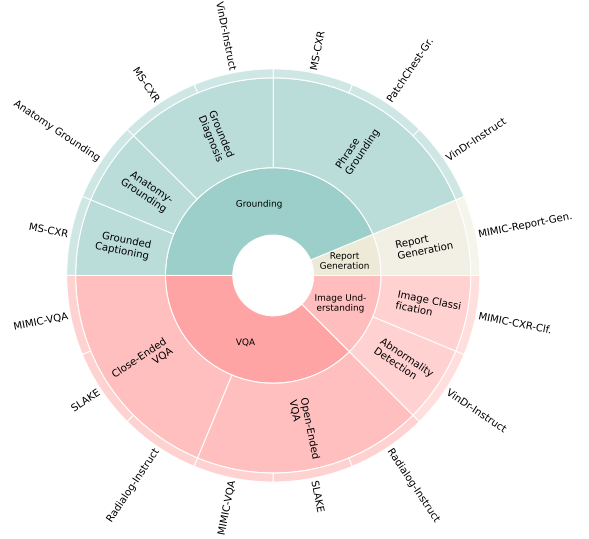


Figure 4. Set of 9 radiology tasks (middle circle) spanning 4 categories (inner circle) done by AnatomicX and the datasets used (outer circle).

step  $t$ ,  $w$  denotes a token in the vocabulary  $V$ , and  $p_{\mathcal{LM}}(w | x_{<t})$  is the probability assigned by  $\mathcal{LM}$  for token  $w$  given  $x_{<t}$ .

## 4. Experiments

**Dataset:** We train APM using over 237,000 samples from the Chest ImaGenome [35] dataset, which extends MIMIC-CXR [14] with detailed spatial and semantic annotations, providing localized information for 36 anatomical objects and their observations. We used the given object-wise phrases for  $S_t$  and the given object bounding boxes for  $y_{box}$  prediction.

Supp. Table S1 provides the summary of nine datasets used for  $\mathcal{LM}$  training. These datasets contain instruction-response pairs derived from eight publicly available CXR datasets including MIMIC-CXR-JPG [14], VinDr-CXR [27], MS-CXR [5], PadChest-Grounding [8], SLAKE [20], MIMIC-CXR-VQA [2], RaDialog-Instruct [28] and Chest-ImaGenome [35]. VinDr-Instruct, and Anatomy Grounding instruction-response datasets were created using the VinDr-CXR [27] and Chest ImaGenome [35] datasets, respectively. Details on these datasets creation are given in the supp. sec. S3.

**Radiology Tasks:** AnatomicX is trained on a diverse set of nine CXR-related tasks, spanning four categories: image understanding, grounding, report generation, and visual question answering (VQA), as illustrated in Fig. 4. Details are provided in the supp. material section S4.

Table 1. Performance on four grounding tasks. For Grounded Diagnosis (GD) and Grounded Captioning (GC), results are shown as GD / GC.

Model	NLG Metrics (GD / GC)			Clinical Metrics (GD / GC)		Phrase Grounding		Anatomy Grounding	
	BERTScore	ROUGE	METEOR	RadGraph-F1	Chexbert-14-F1	IoU	mAP	IoU	mAP
MAIRA-2	0.01 / 0.08	0.01 / 0.06	0.01 / 0.04	0.00 / 0.02	0.03 / 0.02	0.32	0.24	0.35	0.24
RadVLM	0.15 / 0.27	0.06 / 0.11	0.05 / 0.07	0.00 / 0.12	0.32 / 0.40	<u>0.39</u>	<u>0.30</u>	<u>0.60</u>	<u>0.49</u>
CheXagent	<u>0.49 / 0.56</u>	<u>0.43 / 0.44</u>	<u>0.29 / 0.37</u>	<u>0.40 / 0.39</u>	<u>0.40 / 0.61</u>	0.33	0.24	0.18	0.09
<b>AnatomiX (ours)</b>	<b>0.63 / 0.65</b>	<b>0.60 / 0.56</b>	<b>0.42 / 0.48</b>	<b>0.58 / 0.50</b>	<b>0.54 / 0.78</b>	<b>0.46</b>	<b>0.35</b>	<b>0.73</b>	<b>0.66</b>

**Training Scheme:** AnatomiX is trained in three steps that focus on different architectural components and tasks. The first step focuses on the end-to-end training of APM for anatomical object detection and contrastive alignment. We set the number of anatomical objects ( $N$ ) = 36 and train APM for 30 epochs with  $1 \times e^{-4}$  learning rate. Followed by an alignment step (step 2), where we align the embedding space of  $\mathcal{LM}$  and APM by unfreezing the  $\mathcal{P}_{im}$  and  $\mathcal{P}_A$  projectors while keeping all other components frozen. This step uses the report generation dataset for 2 epoch training with  $2 \times e^{-4}$  learning. The third and final step focuses on instruction tuning, where we train  $\mathcal{LM}$  (using LoRA [12]) along with  $\mathcal{P}_{im}$  and  $\mathcal{P}_A$  for 3 epochs while keeping APM frozen. This step includes supervised fine-tuning on all nine tasks discussed in supp. material section S4. All training steps use AdamW [23] optimizer and were trained on 4 NVIDIA H100 GPUs with 80GB memory.

## 5. Results and Discussion

**Grounding:** We begin by evaluating the model’s visual grounding capabilities. Specifically, we examine its ability to highlight relevant regions or pathologies on CXRs and to describe the features present within those regions. This information allows clinicians to visually verify the model’s predictions and gain insight into its decision making process. To assess these capabilities, we evaluate AnatomiX on four challenging grounding tasks using a combination of natural language generation (NLG), clinical, and detection metrics. We primarily compare our model against existing MLLMs with grounding capabilities, including RadVLM [10], Maira-2 [4], and CheXagent [7]. For each compared model, we strictly follow the recommended input-output box coordinates processing scheme for fair comparison.

The phrase grounding and anatomy grounding tasks require localizing entities using bounding boxes. Accordingly, we evaluate these tasks using IoU and mean average precision (mAP) metrics. As shown in Table 1, AnatomiX significantly outperforms all other models by up to 15% in phrase grounding and over 25% in anatomy grounding. This substantial improvement stems from the anatomy-oriented design of AnatomiX, which enables the model to focus more effectively on specific anatomical structures.

Fig. 5 illustrates representative samples of phrase and anatomy grounding tasks, where our model accurately localizes both anatomical regions and pathologies compared to the second best models RadVLM [10] and CheXagent [7]. Detailed anatomy-wise results for anatomy grounding task are given in the supp. Tables S9-S12 (a).

To further evaluate anatomical understanding, we conduct phrase and anatomy grounding tasks on horizontally flipped images, as illustrated in Fig. 1 (c–e). RadVLM [10], the best-performing baseline model, achieves strong results on standard inputs but fails on flipped images, frequently confusing left–right structures and relying on orientation cues. In contrast, AnatomiX maintains accurate grounding under image flipping, demonstrating robust and spatially consistent anatomical reasoning, which is essential for reliable medical image interpretation. Supp. Tables S9-S12 (b–c) present detailed quantitative results, showing that RadVLM performs drops drastically on anatomical objects requiring correct laterality identification e.g., left/right/upper/lower (Tables S10 and S11), with an average overall IoU/mAP of 0.108/0.08. On the contrary, AnatomiX shows no performance degradation in this challenging setting and achieves an average IoU/mAP of 0.712/0.605. Since DL models are prone to shortcut learning and may rely on radiological markers in chest X-rays to infer orientation, we conducted an additional experiment in which radiological markers (e.g., text labels or AP/PA indicators) were manually removed from a subset of images. Manual removal was performed to prevent visual artifacts that could arise from automated editing methods and unintentionally influence model predictions; consequently, only a subset of samples was used in this experiment. As shown in Fig. 6 and supp. Fig. S1, AnatomiX continues to correctly localize diverse anatomical structures and phrases even in the absence of these markers, confirming that its performance is not driven by superficial orientation cues but by genuine anatomical understanding.

The grounded diagnosis and grounded captioning tasks, in contrast, require the model to identify pathologies or describe image content within a user-specified region. We evaluate performance on these tasks using both NLG (ROUGE [19], BERTScore [37], and METEOR [3]) and

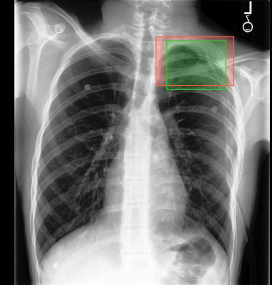
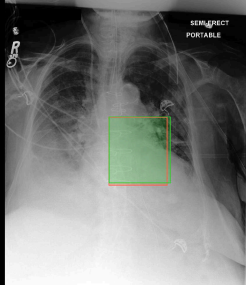
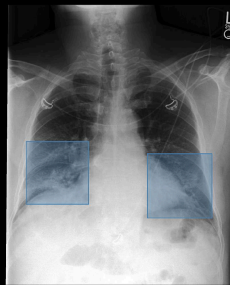
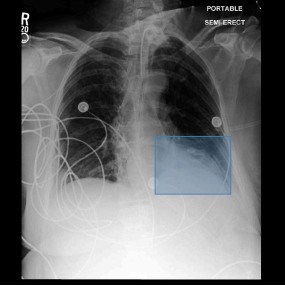
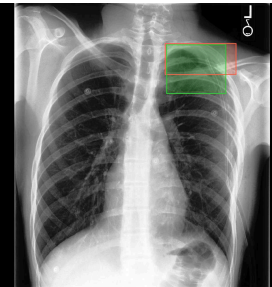
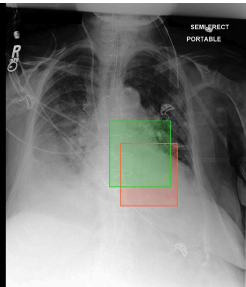
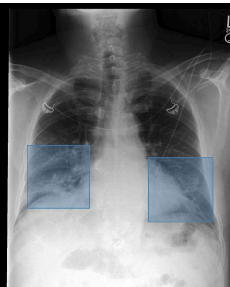
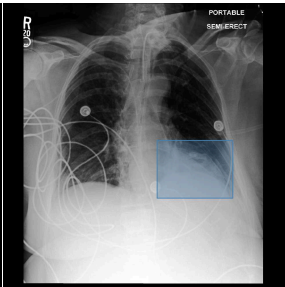
	Phrase Grounding	Anatomy Grounding	Grounded Captioning	Grounded Diagnosis
Prompt	Identify the position of the following finding in the CXR: small left pneumothorax	Where on this image is the Structure of left margin of heart located?	Describe the content of the following region(s): (178,508),(403,735) and (612,552),(845,784)	Please give the corresponding diagnosis for the following region(s): (550,490),(823,699)
AnatomiX (ours)				
	<ref>small left pneumothorax</ref> <box>(560,133),(840,310)</box>	The <ref>Structure of left margin of heart</ref> is at <box>(451,422),(660,667)</box>	Bibasilar pneumonia	Pneumonia
RadVLM / CheXagent				
	This finding is located at [0.58, 0.14, 0.83, 0.25] in the image.	The location for the <ref>Structure of left margin of heart</ref> is marked at [0.48, 0.49, 0.68, 0.71] on the Chest X-ray.	bilateral lower lobe opacities	Pneumothorax
GT	<ref>small left pneumothorax</ref> <box>(598,147),(812,324)</box>	For the <ref>Structure of left margin of heart</ref>, the coordinates are <box>(452,420),(672,658)</box> on the X-ray.	Bibasilar pneumonia	Pneumonia

Figure 5. Sample input-output pairs and comparison with second best models on grounding tasks. The upper panels show outputs from our model across four tasks. The lower panels compare AnatomiX with RadVLM [10] for phrase and anatomy grounding, and with CheXagent [7] for grounded diagnosis and captioning. Box colors: blue = user input, green = ground truth, red = model output.

clinical (RadGraph-F1 [9] and CheXbert-14-F1 [32]) metrics. As shown in Table 1, AnatomiX consistently achieves the highest scores across all metrics providing upto 30% gains in grounded diagnosis and over 25 % improvement in grounded captioning tasks, further underscoring the effectiveness of its anatomy-aware architecture. Fig. 5 show sample input-outputs of AnatomiX and the second best model CheXagent [7] for these two tasks, showcasing our model’s capacity to generate precise and clinically meaningful descriptions aligned with the specified regions. Notably, MAIRA-2 [4] model completely fails to perform these grounding tasks, as it was not trained to incorporate spatial or region-specific input.

**Report Generation:** The automatic generation of radiology reports is an important task that significantly reduces the time required for CXR interpretation and reporting. We evaluate this task using a set of NLG (ROUGE [19], BERTScore [37], METEOR [3]) and clinical (RadGraph-

F1 [9], and CheXbert-14-F1 [32]) metrics. We compare our model against several SOTA CXR report generation models, including RadVLM [10], Maira-2 [4], CheXagent [7], Radialog [28], and Medgamma [31]. Table 2 shows that AnatomiX consistently outperforms competing approaches across metrics, demonstrating its strong capability in producing both linguistically coherent and clinically accurate reports. The only exception occurs in CheXbert-14-F1 [32], where AnatomiX attains an F1 score of 0.42, compared

Table 2. NLG and Clinical metrics for Report Generation task.

Model	NLG Metrics			Clinical Metrics	
	ROUGE	BERTScore	METEOR	RadGraph	CheXbert-14 F1
MAIRA-2	0.43	0.25	0.12	0.17	0.45
Radialog	0.51	0.35	0.18	0.24	0.48
MedGamma	0.37	0.29	0.18	0.20	0.40
RadVLM	0.45	0.27	0.12	0.19	0.32
CheXagent	0.32	0.16	0.06	0.15	0.31
<b>AnatomiX (ours)</b>	<b>0.53</b>	<b>0.38</b>	<b>0.21</b>	<b>0.26</b>	0.42

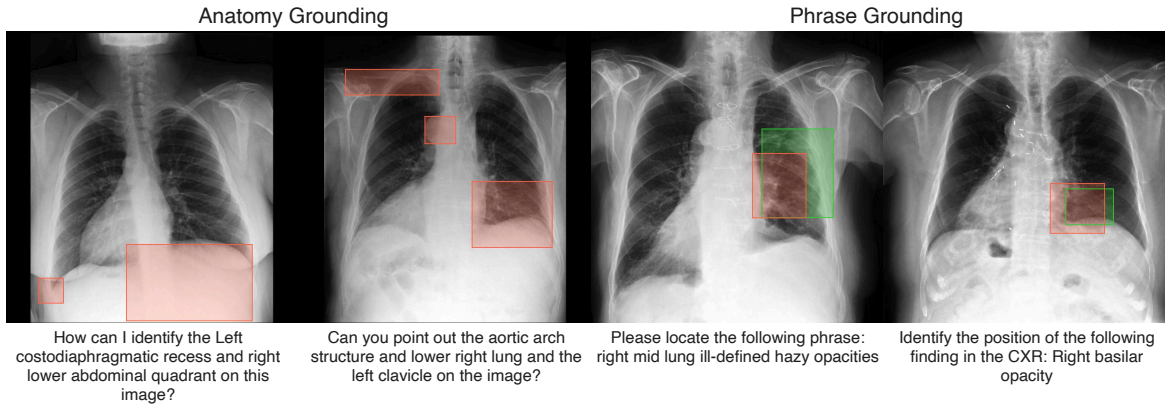


Figure 6. AnATOMiX output for anatomy and phrase grounding on flipped images (left ↔ right) with radiographic markers removed.

Table 3. Performance on image classification and detection tasks.

Model	Classification	Detection	
	CheXbert-14 F1	IoU	mAP
MAIRA-2	0.00	0.16	0.01
Radialog	0.47	0.00	0.00
MedGemma	0.40	0.04	0.00
RadVLM	0.43	0.28	0.12
CheXagent	0.85	0.31	0.22
<b>AnATOMiX (ours)</b>	<b>0.85</b>	<b>0.31</b>	<b>0.20</b>

to 0.48 for Radialog and 0.45 for Maira-2. Importantly, both of these models contain approximately  $1.5 \times$  more parameters than AnATOMiX, emphasizing the efficiency and scalability of our approach. These results collectively highlight AnATOMiX’s balance between performance and computational efficiency, suggesting that it effectively captures domain-specific medical semantics without relying on excessively large model architectures.

### Image Understanding and Visual Question Answering (VQA):

For image understanding tasks (image classification and abnormality detection) we evaluate using CheXbert-14-F1 [32], IoU, and mAP. AnATOMiX outperforms all compared models in classification, achieves the highest IoU for abnormality detection, and maintains competitive mAP performance, highlighting strong visual reasoning and reliable localization (Table 3). For VQA, we benchmark on open- and close-ended tasks using BERTScore [37] and CheXbert-14-F1. AnATOMiX demonstrates strong performance across both settings (Table 4), outperforming all models and matching or exceeding CheXagent [7]. Minor score differences mainly arise from keyword mismatches with ground truth—for example, when the answer to “*Is there any pneumonia in the image?*” is “*yes, pneumonia is present*” but the model outputs “*yes*”, or vice versa—leading to lower metric scores despite clinical correctness. Overall, these results highlight AnATOMiX’s

Table 4. Open and close ended VQA task performance.

Model	Open-Ended VQA		Close-Ended VQA	
	BERTScore	CheXbert-14 F1	BERTScore	CheXbert-14 F1
MAIRA-2	0.07	0.31	0.10	0.81
Radialog	0.08	0.43	0.03	0.92
MedGemma	0.03	0.44	0.02	0.38
RadVLM	0.07	0.04	0.23	0.67
CheXagent	0.86	0.87	0.90	0.97
<b>AnATOMiX (ours)</b>	<b>0.86</b>	<b>0.86</b>	<b>0.89</b>	<b>0.95</b>

strong image understanding and high VQA capabilities.

## 6. Conclusion and Future Work

In conclusion, AnATOMiX shows significant improvements in CXR interpretation, especially in tasks that require a direct anatomical understanding. Our results highlight that anatomy-oriented design is the key to accurate spatial reasoning in medical MLLMs. While simple finetuning natural image MLLMs on large medical datasets can help, it can create false spatial correspondences. Future work could extend anatomy oriented architectures to other modalities such as MRI and improve the current architecture by reducing the potential redundancy multi-modal prompt. Furthermore, this study focuses on single turn interactions; extending it to multi turn setups would enhance flexibility and applicability. Overall, this work marks an important step toward domain-specific design in MLLMs.

**Acknowledgment:** This work was supported in part through the Minerva computational and data resources [16] and staff expertise provided by Scientific Computing and Data at the Icahn School of Medicine at Mount Sinai and supported by the Clinical and Translational Science Awards (CTSA) grant UL1TR004419 from the National Centre for Advancing Translational Sciences.

## References

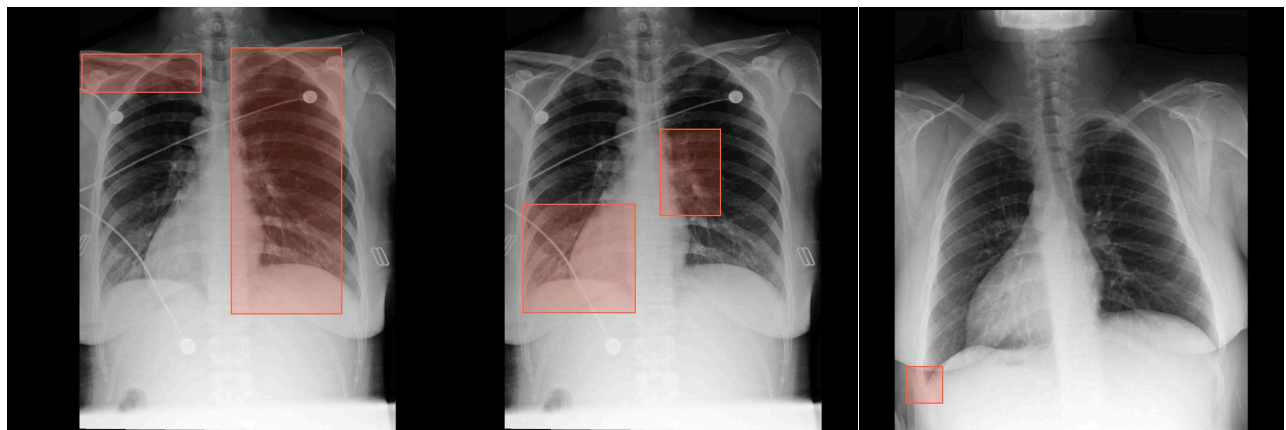
- [1] DM Anisuzzaman, Jeffrey G Malins, Paul A Friedman, and Zachi I Attia. Fine-tuning llms for specialized use cases. *Mayo Clinic Proceedings: Digital Health*, 2024. 1
- [2] Seongsu Bae, Daeun Kyung, Jaehee Ryu, Eunbyeol Cho, Gyubok Lee, Sunjun Kweon, Jungwoo Oh, Lei Ji, Eric Chang, Tackeun Kim, et al. Mimic-ext-mimic-cxr-vqa: A complex, diverse, and large-scale visual question answering dataset for chest x-ray images, 2024. 5
- [3] Satanjeev Banerjee and Alon Lavie. Meteor: An automatic metric for mt evaluation with improved correlation with human judgments. In *Proceedings of the acl workshop on intrinsic and extrinsic evaluation measures for machine translation and/or summarization*, pages 65–72, 2005. 6, 7
- [4] Shruthi Bannur, Kenza Bouzid, Daniel C Castro, Anton Schwaighofer, Anja Thieme, Sam Bond-Taylor, Maximilian Ilse, Fernando Pérez-García, Valentina Salvatelli, Harshita Sharma, et al. Maira-2: Grounded radiology report generation. *arXiv preprint arXiv:2406.04449*, 2024. 1, 2, 6, 7
- [5] Benedikt Boecking, Naoto Usuyama, Shruthi Bannur, Daniel C Castro, Anton Schwaighofer, Stephanie Hyland, Maria Wetscherek, Tristan Naumann, Aditya Nori, Javier Alvarez-Valle, et al. Making the most of text semantics to improve biomedical vision–language processing. In *European conference on computer vision*, pages 1–21. Springer, 2022. 5
- [6] Nicolas Carion, Francisco Massa, Gabriel Synnaeve, Nicolas Usunier, Alexander Kirillov, and Sergey Zagoruyko. End-to-end object detection with transformers. In *European conference on computer vision*, pages 213–229. Springer, 2020. 3
- [7] Zhihong Chen, Maya Varma, Jean-Benoit Delbrouck, Magdalini Paschali, Louis Blankemeier, Dave Van Veen, Jeya Maria Jose Valanarasu, Alaa Youssef, Joseph Paul Cohen, Eduardo Pontes Reis, et al. Chexagent: Towards a foundation model for chest x-ray interpretation. *arXiv preprint arXiv:2401.12208*, 2024. 1, 2, 6, 7, 8
- [8] Daniel Coelho de Castro, Aurelia Bustos, Shruthi Bannur, Stephanie L Hyland, Kenza Bouzid, Maria Teodora Wetscherek, Maria Dolores Sánchez-Valverde, Lara Jaques-Pérez, Lourdes Pérez-Rodríguez, Kenji Takeda, et al. Padchest-gr: A bilingual chest x-ray dataset for grounded radiology report generation. *NEJM AI*, 2(7):A1dbp2401120, 2025. 5
- [9] Jean-Benoit Delbrouck, Pierre Chambon, Christian Bluethgen, Emily Tsai, Omar Almusa, and Curtis P Langlotz. Improving the factual correctness of radiology report generation with semantic rewards. *arXiv preprint arXiv:2210.12186*, 2022. 7
- [10] Nicolas Deperrois, Hidetoshi Matsuo, Samuel Ruipérez-Campillo, Moritz Vandenheert, Sonia Laguna, Alain Ryser, Koji Fujimoto, Mizuho Nishio, Thomas M Sutter, Julia E Vogt, et al. Radvlm: A multitask conversational vision-language model for radiology. *arXiv preprint arXiv:2502.03333*, 2025. 1, 2, 6, 7
- [11] Yu Gu, Robert Tinn, Hao Cheng, Michael Lucas, Naoto Usuyama, Xiaodong Liu, Tristan Naumann, Jianfeng Gao, and Hoifung Poon. Domain-specific language model pre-training for biomedical natural language processing. *ACM Transactions on Computing for Healthcare (HEALTH)*, 3(1): 1–23, 2021. 4
- [12] Edward J Hu, Yelong Shen, Phillip Wallis, Zeyuan Allen-Zhu, Yuanzhi Li, Shean Wang, Lu Wang, Weizhu Chen, et al. Lora: Low-rank adaptation of large language models. *ICLR*, 1(2):3, 2022. 5, 6
- [13] Ding Jiang and Mang Ye. Cross-modal implicit relation reasoning and aligning for text-to-image person retrieval. In *Proceedings of the IEEE/CVF conference on computer vision and pattern recognition*, pages 2787–2797, 2023. 4
- [14] Alistair EW Johnson, Tom J Pollard, Seth J Berkowitz, Nathaniel R Greenbaum, Matthew P Lungren, Chih-ying Deng, Roger G Mark, and Steven Horng. Mimic-cxr, a de-identified publicly available database of chest radiographs with free-text reports. *Scientific data*, 6(1):317, 2019. 5
- [15] Alexander Kirillov, Eric Mintun, Nikhila Ravi, Hanzi Mao, Chloe Rolland, Laura Gustafson, Tete Xiao, Spencer Whitehead, Alexander C Berg, Wan-Yen Lo, et al. Segment anything. In *Proceedings of the IEEE/CVF international conference on computer vision*, pages 4015–4026, 2023. 2
- [16] P. Kovatch, L. Gai, H. M. Cho, E. Fluder, and D. Jiang. Optimizing high-performance computing systems for biomedical workloads. In *Proceedings of the IEEE International Symposium on Parallel and Distributed Processing Workshops (IPDPSW) PhD Forum*, pages 183–192, 2020. Epub 2020-07-28. 8
- [17] Chunyuan Li, Cliff Wong, Sheng Zhang, Naoto Usuyama, Haotian Liu, Jianwei Yang, Tristan Naumann, Hoifung Poon, and Jianfeng Gao. Llava-med: Training a large language-and-vision assistant for biomedicine in one day. *Advances in Neural Information Processing Systems*, 36:28541–28564, 2023. 2
- [18] Qingqiu Li, Zihang Cui, Seongsu Bae, Jilan Xu, Runtian Yuan, Yuejie Zhang, Rui Feng, Quanli Shen, Xiaobo Zhang, Junjun He, et al. Aor: Anatomical ontology-guided reasoning for medical large multimodal model in chest x-ray interpretation. *arXiv preprint arXiv:2505.02830*, 2025. 2
- [19] Chin-Yew Lin. Rouge: A package for automatic evaluation of summaries. In *Text summarization branches out*, pages 74–81, 2004. 6, 7
- [20] Bo Liu, Li-Ming Zhan, Li Xu, Lin Ma, Yan Yang, and Xiao-Ming Wu. Slake: A semantically-labeled knowledge-enhanced dataset for medical visual question answering. In *2021 IEEE 18th international symposium on biomedical imaging (ISBI)*, pages 1650–1654. IEEE, 2021. 5
- [21] Haotian Liu, Chunyuan Li, Qingyang Wu, and Yong Jae Lee. Visual instruction tuning. *Advances in neural information processing systems*, 36:34892–34916, 2023. 1, 2
- [22] Jingping Liu, Ziyang Liu, Zhedong Cen, Yan Zhou, Yinan Zou, Weiyan Zhang, Haiyun Jiang, and Tong Ruan. Can multimodal large language models understand spatial relations? *arXiv preprint arXiv:2505.19015*, 2025. 1
- [23] Ilya Loshchilov and Frank Hutter. Decoupled weight decay regularization. *arXiv preprint arXiv:1711.05101*, 2017. 6
- [24] Lingxiao Luo, Bingda Tang, Xuanzhong Chen, Rong Han, and Ting Chen. Vividmed: Vision language model with

- versatile visual grounding for medicine. *arXiv preprint arXiv:2410.12694*, 2024. 1, 2
- [25] Chuofan Ma, Yi Jiang, Jiannan Wu, Zehuan Yuan, and Xiaojuan Qi. Groma: Localized visual tokenization for grounding multimodal large language models. In *European Conference on Computer Vision*, pages 417–435. Springer, 2024. 1
- [26] Philip Müller, Georgios Kaissis, and Daniel Rueckert. Chex: Interactive localization and region description in chest x-rays. In *European Conference on Computer Vision*, pages 92–111. Springer, 2024. 2
- [27] Ha Q Nguyen, Khanh Lam, Linh T Le, Hieu H Pham, Dat Q Tran, Dung B Nguyen, Dung D Le, Chi M Pham, Hang TT Tong, Diep H Dinh, et al. Vindr-cxr: An open dataset of chest x-rays with radiologist’s annotations. *Scientific Data*, 9(1):429, 2022. 5
- [28] Chantal Pellegrini, Ege Özsoy, Benjamin Busam, Nassir Navab, and Matthias Keicher. Radialog instruct dataset. 2, 5, 7
- [29] Zhiliang Peng, Wenhui Wang, Li Dong, Yaru Hao, Shaohan Huang, Shuming Ma, and Furu Wei. Kosmos-2: Grounding multimodal large language models to the world. *arXiv preprint arXiv:2306.14824*, 2023. 1
- [30] Alec Radford, Jong Wook Kim, Chris Hallacy, Aditya Ramesh, Gabriel Goh, Sandhini Agarwal, Girish Sastry, Amanda Askell, Pamela Mishkin, Jack Clark, et al. Learning transferable visual models from natural language supervision. In *International conference on machine learning*, pages 8748–8763. PmLR, 2021. 4
- [31] Andrew Sellergren, Sahar Kazemzadeh, Tiam Jaroensri, Atilla Kiraly, Madeleine Traverse, Timo Kohlberger, Shawn Xu, Fayaz Jamil, Cían Hughes, Charles Lau, et al. Medgemma technical report. *arXiv preprint arXiv:2507.05201*, 2025. 2, 5, 7
- [32] Akshay Smit, Saahil Jain, Pranav Rajpurkar, Anuj Pareek, Andrew Y Ng, and Matthew P Lungren. Chexbert: combining automatic labelers and expert annotations for accurate radiology report labeling using bert. *arXiv preprint arXiv:2004.09167*, 2020. 7, 8
- [33] Andrew Szot, Bogdan Mazouze, Harsh Agrawal, R Devon Hjelm, Zsolt Kira, and Alexander Toshev. Grounding multimodal large language models in actions. *Advances in Neural Information Processing Systems*, 37:20198–20224, 2024. 1
- [34] Daniel Wolf, Heiko Hillenhausen, Billurvan Taskin, Alex Bäuerle, Meinrad Beer, Michael Götz, and Timo Ropinski. Your other left! vision-language models fail to identify relative positions in medical images. In *International Conference on Medical Image Computing and Computer-Assisted Intervention*, pages 691–701. Springer, 2025. 1, 3
- [35] Joy T Wu, Nkechinyere N Agu, Ismini Lourentzou, Arjun Sharma, Joseph A Paguio, Jasper S Yao, Edward C Dee, William Mitchell, Satyananda Kashyap, Andrea Giovannini, et al. Chest imagenome dataset for clinical reasoning. *arXiv preprint arXiv:2108.00316*, 2021. 5
- [36] Hanguang Xiao, Feizhong Zhou, Xingyue Liu, Tianqi Liu, Zhipeng Li, Xin Liu, and Xiaoxuan Huang. A comprehensive survey of large language models and multimodal large language models in medicine. *Information Fusion*, page 102888, 2024. 1
- [37] Tianyi Zhang, Varsha Kishore, Felix Wu, Kilian Q Weinberger, and Yoav Artzi. Bertscore: Evaluating text generation with bert. *arXiv preprint arXiv:1904.09675*, 2019. 6, 7, 8
- [38] Ke Zou, Yang Bai, Zhihao Chen, Yang Zhou, Yidi Chen, Kai Ren, Meng Wang, Xuedong Yuan, Xiaojing Shen, and Huazhu Fu. Medrg: Medical report grounding with multi-modal large language model. *arXiv preprint arXiv:2404.06798*, 2024. 2

# AnatomiX, an Anatomy-Aware Grounded Multimodal Large Language Model for Chest X-Ray Interpretation

## Supplementary Material

### Anatomy Grounding

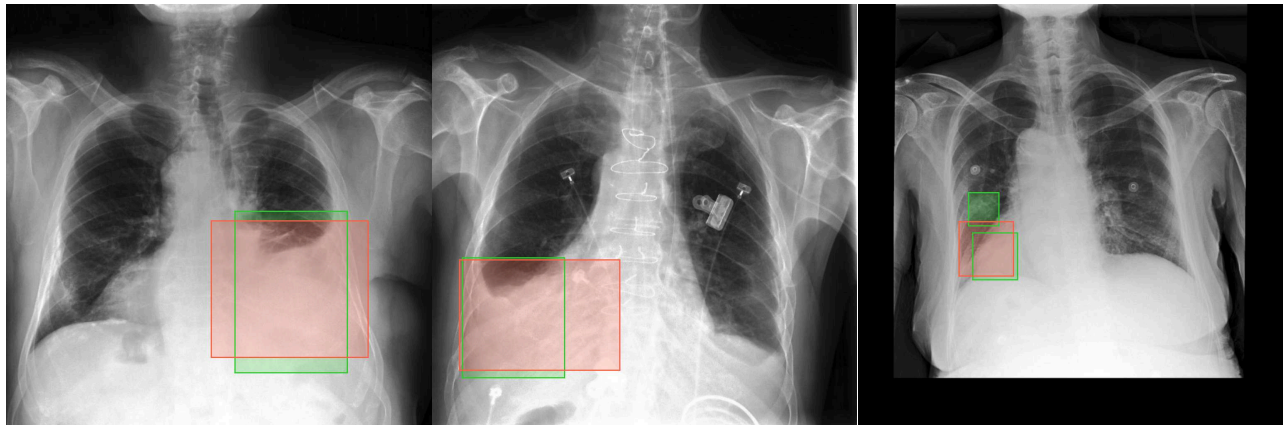


Can you point out the left clavical and right lung position on the image?

Point out the exact location of the Hilar area of right lung and the left lower lung zone.

How can I identify the Left costodiaphragmatic recess on this image?

### Phrase Grounding



Identify the position of the following finding in the CXR: right pleural effusion with probable superimposed atelectasis

Identify the position of the following finding in the CXR: Small to moderate left-sided pleural effusion

Identify the position of the following finding in the CXR: possible small area of consolidation in the left lower lobe

Figure S1. Additional samples for AnatomiX's output for anatomy and phrase grounding on flipped images (left ↔ right) with radiographic markers removed. Bottom: Green boxes show the ground truth, while red show the model prediction.

## Multimodal Prompt

**User:**

You are a professional radiologist. I will provide you with context containing likely features about different parts of the chest X-rays.

**Image:**

<image\_start> <image> ... <image> <image\_end>

**Likely findings:**

<emb><obj\_0></emb> <box>(0,387), (670,1024)</box> Abdominal cavity shows enteric tube.

<emb><obj\_1></emb> <box>(300,118), (394,207)</box> Aortic arch structure is healthy.

...

<emb><obj\_N></emb> <box>(398,391), (517,518)</box> Right cardiophrenic sulcus is healthy.

**Task:** [TASK]

**Model Response:** [MODEL RESPONSE]

Figure S2. Multimodal prompt template used in  $\mathcal{LM}$ . Colored tags (<emb> and <box>) denote special tokens corresponding to anatomical object embeddings and bounding boxes, respectively. Each <obj\_i> token represents the embedding of the  $i^{\text{th}}$  anatomical object, while <image> indicates image patch embeddings.

## S1. Self-Similarity Loss Matrix

The Contrastive Alignment stage of the Anatomy Perception Module (APM) utilizes the Self-Similarity matrix  $S_{self}$  to model fine grained semantic relations among anatomical descriptions. In this stage, a pretrained sentence encoder  $\mathcal{S}$  provides indirect supervision by embedding textual inputs into a continuous semantic space that captures linguistic and clinical similarities. Given a set of input sentences  $S_t$ , each sentence is encoded through  $\mathcal{S}$  to obtain text embeddings  $S_E \in \mathbb{R}^{N \times 768}$ , where each row corresponds to the representation of one sentence in a 768-dimensional embedding space. To ensure consistency and comparability across representations, the embeddings are first normalized using  $\ell_2$  normalization:

$$\bar{S}_E = \frac{S_E}{|S_E|_2} \quad (S1)$$

This normalization projects the embeddings onto a unit hypersphere, ensuring that they encode directional (semantic) differences rather than magnitude based variations. The normalized embeddings are then used to compute the Self-Similarity matrix:

$$S_{self} = \text{Softmax}(\bar{S}_E) \cdot \text{Softmax}(\bar{S}_E)^T \quad (S2)$$

where  $S_{self} \in \mathbb{R}^{N \times N}$  encodes pairwise similarity scores between all sentences in  $S_t$ . The softmax operation (applied row wise) ensures these similarities are smooth and probabilistically interpretable.

Next, to align anatomical and textual semantics, we compute a projected similarity matrix  $\hat{K}_A$  between the projected anatomical features  $\hat{O}_A$  and projected text embeddings  $\hat{S}_A$ :

$$\hat{K}_A = \text{Softmax} \left( \frac{\hat{O}_A \hat{S}_A^T}{\tau} \right) \quad (S3)$$

where  $\hat{K}_A \in \mathbb{R}^{N \times N}$ , and  $\tau$  is the temperature coefficient (set to 0.01) that controls the sharpness of the similarity distribution.

The final contrastive alignment loss is defined as the averaged KL-divergence between the anatomical-textual similarity matrix  $\hat{K}_A$  and the self-similarity matrix  $S_{self}$ , computed in both row-wise and column-wise directions to enforce mutual consistency:

$$\mathcal{L}_{CL} = \frac{1}{2} KL \left( \hat{K}_A, S_{self} \right) + \frac{1}{2} KL \left( \hat{K}_A^T, S_{self}^T \right) \quad (S4)$$

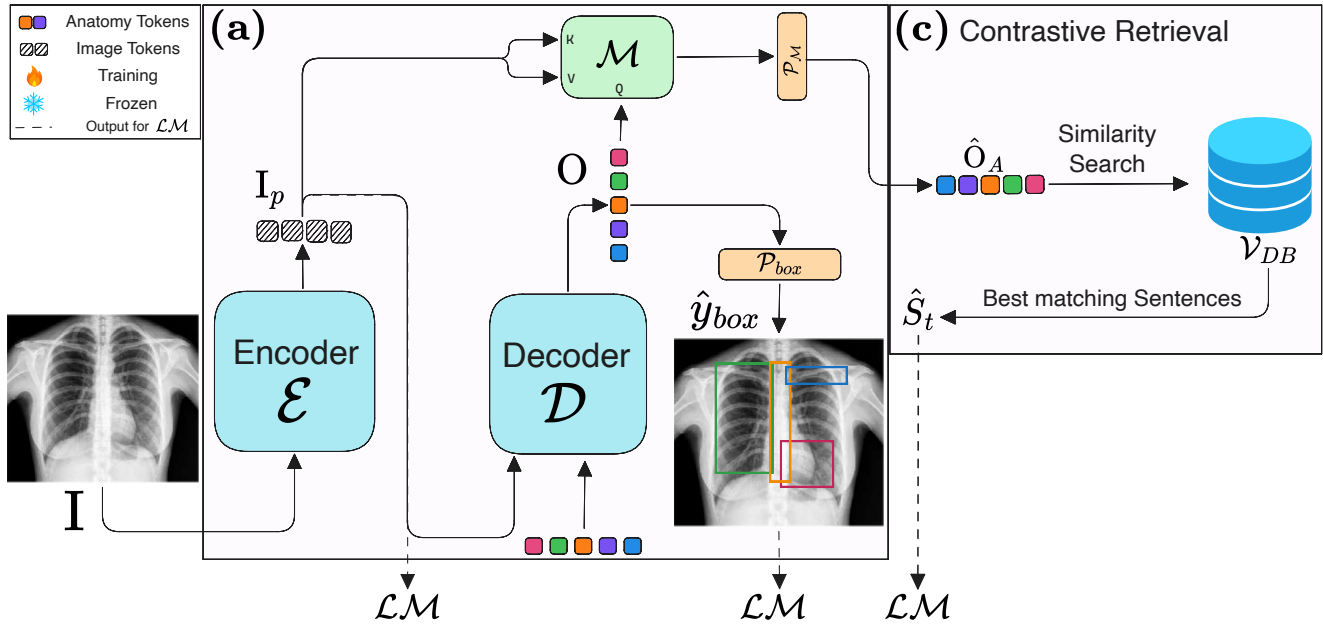


Figure S3. APM architecture during inference, where the Contrastive Alignment’s components are replaced with vector database for the Contrastive Retrieval. See Fig. 2 for training architecture.

This formulation encourages  $\hat{O}_A$  and  $\hat{S}_A$  to maintain pairwise relationships that reflect the semantic structure captured in  $S_{self}$ . As a result, the APM preserves semantic coherence and clinical consistency across related sentences, capturing overlapping anatomical features rather than enforcing strict one-to-one alignments.

## S2. Vector Database

During APM inference, we replace the Contrastive Alignment with the Contrastive Retrieval (see Fig. S3) to identify the semantically most similar sentences to the anatomical object tokens  $\hat{O}_A$ . These retrieved sentences represent the most probable observations for each anatomical object and thus provide important contextual information for downstream descriptive tasks in  $\mathcal{LM}$ , as discussed in ablations.

The vector database, denoted as  $\mathcal{V}_{DB}$ , stores all unique sentences associated with each anatomical object from the validation set of the Chest-ImaGenome dataset. For every object in an image, we construct a concise descriptive sentence using the corresponding phrases and attributes given in the original dataset (example sentence: “Right lower lung shows pleural effusion and atelectasis”). To build  $\mathcal{V}_{DB}$ , we first compile the set of unique sentences for each anatomical object. Each sentence is then encoded using the sentence encoder  $\mathcal{S}$  and the trained projection head  $\mathcal{P}_S$ , producing  $s$ -dimensional embeddings (see Fig. 2 for  $\mathcal{P}_S$ ). These embeddings, along with their corresponding sentences, are stored as key–value pairs in  $\mathcal{V}_{DB}$ , with a distinct sub-database allocated to each anatomical object. Consequently,  $\mathcal{V}_{DB}$  comprises  $N$  independent sub-databases. The full distribution for the size of each anatomical object database is shown in Fig. S4.

The compact nature of both the embeddings and the sentences ensures that  $\mathcal{V}_{DB}$  remains lightweight, enabling efficient retrieval at inference time. During inference, a similarity search is performed between each anatomical object token  $\hat{O}_A^i$  and the sentence embeddings within the corresponding sub-database of  $\mathcal{V}_{DB}$ , thereby retrieving the most relevant descriptive sentences for each object. These sentences are then passed to  $\mathcal{LM}$  using a multimodal prompt template shown in Fig. S2, where they provide important contextual information about each anatomy.

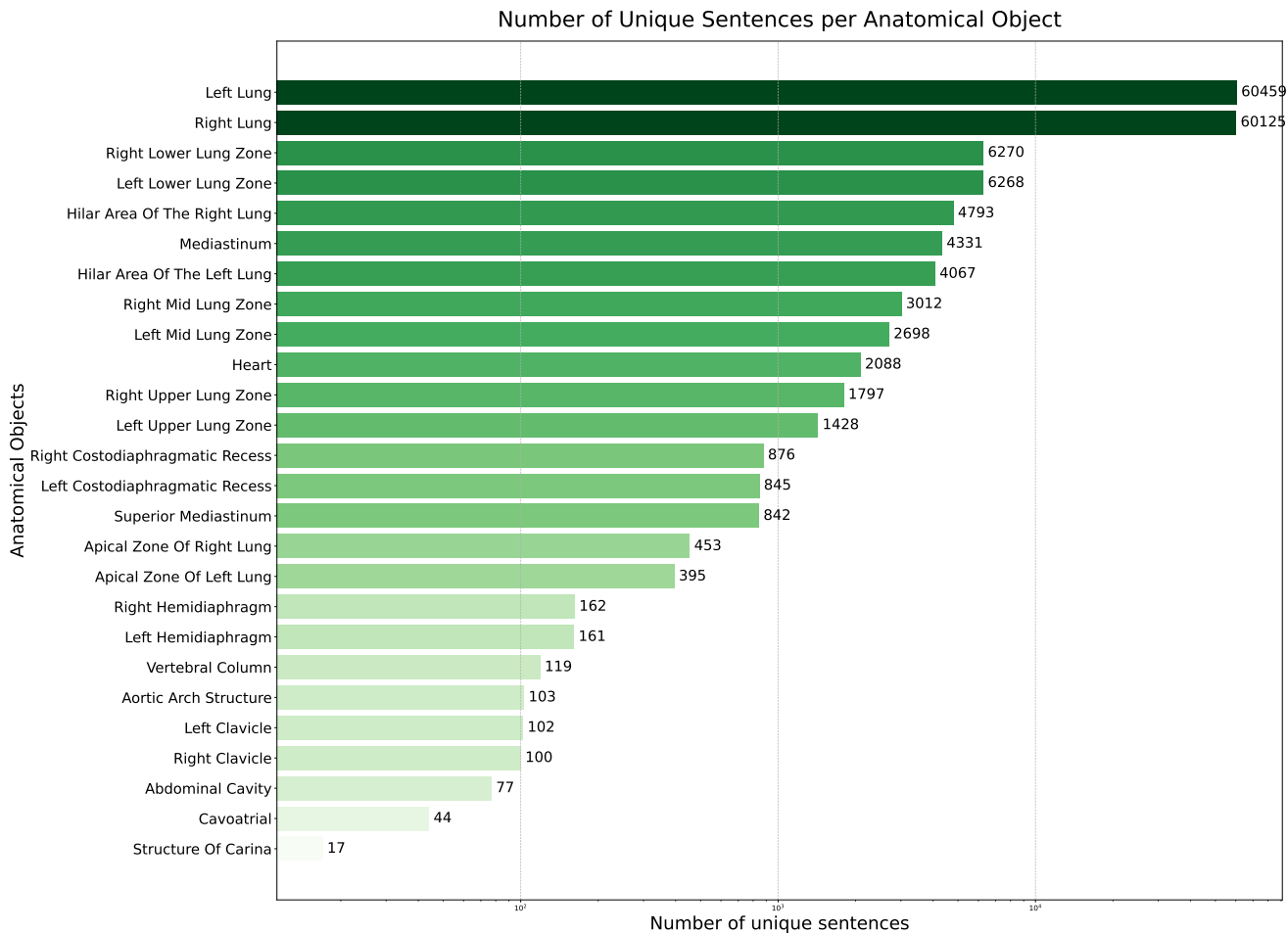


Figure S4. Size of the vector database. Each bar shows the number of unique sentences associated with a specific anatomical object. Anatomical objects with fewer than 10 unique sentences are omitted for clarity.

## S3. Datasets

### S3.1. Anatomy Grounding

For instruction tuning, we construct the Anatomy Grounding dataset using bounding box annotations for 36 distinct anatomical structures. We design 20 question and answer templates, as illustrated in Fig. S5. The question templates query the location of a specific anatomical structure, while the answer templates include both the anatomical name and its location (i.e., bounding box coordinates). During dataset construction, we randomly sample from the question and answer templates to increase data diversity. The final dataset contains the same number of samples as Chest-ImaGenome, maintains a uniform distribution of anatomical structures, and follows the official data split of Chest-ImaGenome.

### S3.2. VinDr-Instruct

The VinDr-Instruct dataset is constructed from the VinDr-CXR dataset and comprises question–answer pairs for abnormality detection, phrase grounding, and grounded diagnosis tasks. We adopt the question templates proposed in CheXagent, as illustrated in Fig. S6. The answers are formatted as single- or multi-word responses that contain only the essential information, without full sentence structures. In this work, we follow the original train–test split of the VinDr-CXR dataset.

## Templates for VinDr-Instruct

### Questions:

- Where is the {anatomy} located in this Chest X-ray?
- Can you point out the {anatomy}'s position on the image?
- What's the location of the {anatomy} in the X-ray?
- Identify where the {anatomy} is on this Chest X-ray, please.
- Where exactly is the {anatomy} found on this image?
- Could you specify where to find the {anatomy} on this X-ray?
- Highlight the {anatomy}'s area on the image.
- Show me the {anatomy}'s location on this CXR.
- Where should I look to find the {anatomy} in this image?
- Can you locate the {anatomy} on this X-ray for me?
- Please point to the {anatomy} on this Chest X-ray.
- Indicate the position of the {anatomy} on this image.
- Describe the location of the {anatomy} on the X-ray.
- Where on this image is the {anatomy} located?
- Point out the exact location of the {anatomy} in the Chest X-ray.
- How can I identify the {anatomy} on this image?
- Where is the {anatomy} situated in this CXR?
- Can you highlight the {anatomy} on this image?
- Indicate where the {anatomy} is found on this X-ray.
- Describe where to find the {anatomy} on this Chest X-ray.

### Answers:

- The {ref<sub>i</sub>{anatomy}}/{ref<sub>i</sub>} is located at the coordinates {box<sub>i</sub>{boxes}}/{box<sub>i</sub>} on the image.
- You'll find the {ref<sub>i</sub>{anatomy}}/{ref<sub>i</sub>} at {box<sub>i</sub>{boxes}}/{box<sub>i</sub>} in the X-ray.
- The {ref<sub>i</sub>{anatomy}}/{ref<sub>i</sub>} can be seen at {box<sub>i</sub>{boxes}}/{box<sub>i</sub>} on the Chest X-ray.
- The location of the {ref<sub>i</sub>{anatomy}}/{ref<sub>i</sub>} is at {box<sub>i</sub>{boxes}}/{box<sub>i</sub>} on the image.
- For the {ref<sub>i</sub>{anatomy}}/{ref<sub>i</sub>}, the coordinates are {box<sub>i</sub>{boxes}}/{box<sub>i</sub>} on the X-ray.
- The {ref<sub>i</sub>{anatomy}}/{ref<sub>i</sub>} is situated at {box<sub>i</sub>{boxes}}/{box<sub>i</sub>} in the image.
- On the Chest X-ray, the {ref<sub>i</sub>{anatomy}}/{ref<sub>i</sub>} is located at {box<sub>i</sub>{boxes}}/{box<sub>i</sub>}
- The {ref<sub>i</sub>{anatomy}}/{ref<sub>i</sub>} appears at the coordinates {box<sub>i</sub>{boxes}}/{box<sub>i</sub>} on the image.
- In the X-ray, the {ref<sub>i</sub>{anatomy}}/{ref<sub>i</sub>} is identifiable at {box<sub>i</sub>{boxes}}/{box<sub>i</sub>}.
- The location for the {ref<sub>i</sub>{anatomy}}/{ref<sub>i</sub>} is marked at {box<sub>i</sub>{boxes}}/{box<sub>i</sub>} on the Chest X-ray.
- The {ref<sub>i</sub>{anatomy}}/{ref<sub>i</sub>} is positioned at {box<sub>i</sub>{boxes}}/{box<sub>i</sub>} on the image.
- The area occupied by the {ref<sub>i</sub>{anatomy}}/{ref<sub>i</sub>} is at {box<sub>i</sub>{boxes}}/{box<sub>i</sub>} in the X-ray.
- On the image, you can find the {ref<sub>i</sub>{anatomy}}/{ref<sub>i</sub>} at {box<sub>i</sub>{boxes}}/{box<sub>i</sub>}.
- The {ref<sub>i</sub>{anatomy}}/{ref<sub>i</sub>}'s location is at {box<sub>i</sub>{boxes}}/{box<sub>i</sub>} on the Chest X-ray.
- In terms of coordinates, the {ref<sub>i</sub>{anatomy}}/{ref<sub>i</sub>} is found at {box<sub>i</sub>{boxes}}/{box<sub>i</sub>} on the image.
- Regarding the {ref<sub>i</sub>{anatomy}}/{ref<sub>i</sub>}, it is located at {box<sub>i</sub>{boxes}}/{box<sub>i</sub>} on the X-ray.
- The {ref<sub>i</sub>{anatomy}}/{ref<sub>i</sub>} specifically is at {box<sub>i</sub>{boxes}}/{box<sub>i</sub>} on the Chest X-ray.
- Concerning the {ref<sub>i</sub>{anatomy}}/{ref<sub>i</sub>}, you will find it at {box<sub>i</sub>{boxes}}/{box<sub>i</sub>} in the image.
- The {ref<sub>i</sub>{anatomy}}/{ref<sub>i</sub>} is at {box<sub>i</sub>{boxes}}/{box<sub>i</sub>} on the X-ray.
- For identifying the {ref<sub>i</sub>{anatomy}}/{ref<sub>i</sub>}, look at {box<sub>i</sub>{boxes}}/{box<sub>i</sub>} on the Chest X-ray.

Figure S5. Instruction QA templates for Anatomy Grounding dataset. {anatomy} and {boxes} represents the Anatomy name and location (coordinates), respectively.

## Templates for VinDr-Instruct

### Abnormality Detection:

- Detect {disease} in the given image.
- Locate areas in the chest X-ray where {disease} are present, using bounding box coordinates
- Perform abnormality detection (in the bounding box format) for the given image.
- Find the locations of {disease} in the bounding box format for the given image.
- Locate {disease} for the given image.
- Examine the chest X-ray and mark the regions affected by {disease} with bounding boxes.
- Detect the following in the image: {disease}.
- Examine the image for regions affected by {disease}, and indicate their positions with bounding boxes.
- Perform detection for {disease}.

### Phrase Grounding:

- Detect {disease} in the given image.
- Locate areas in the chest X-ray where {disease} is present, using bounding box coordinates.
- Localize {disease} in the bounding box format for the given image.
- Find the locations of {disease} in the bounding box format for the given image.
- Locate {disease} for the given image.
- Examine the chest X-ray and mark the regions affected by {disease} with bounding boxes.
- Detect the following in the image: {disease}.
- Examine the image for regions affected by {disease}, and indicate their positions with bounding boxes.
- Perform detection for {disease}.

### Grounded Diagnosis:

- Please give the corresponding diagnosis for the following region(s): {boxes}
- Provide a diagnosis based on the content of the following region(s): {boxes}

Figure S6. Instruction templates used for generating VinDr-Instruct dataset. {disease} and {boxes} represents the input abnormality name and box coordinates, respectively.

Table S1. Number of training, validation, and test samples for the nine datasets used in  $\mathcal{LM}$  training and validation. The Source column indicates the original public dataset used directly or as the basis for dataset creation.

Dataset	Source	Test	Train	Val
MIMIC-VQA	MIMIC-CXR-VQA	5,497	101,963	4,926
RaDialog Instruct	RaDialog Instruct	799	6,274	822
SLAKE	SLAKE	298	1,175	285
Anatomy Grounding	Chest-ImaGenome	3,403	237,938	1,959
MS-CXR	MS-CXR	528	2,445	507
VinDr-Instruct	VinDr-CXR	6,166	38,122	4,099
PadChest-Grounding	PadChest-Grounding	1,121	3,920	558
MIMIC-CXR Classification	MIMIC-CXR	2,957	182,425	1,666
MIMIC Report Gen	MIMIC-CXR	1,722	135,049	1,078
<b>Total</b>	–	<b>22,491</b>	<b>709,311</b>	<b>15,900</b>

## S4. Radiology Tasks

Anatomix is trained and evaluated on nine CXR-related tasks, spanning four categories: image understanding, grounding, report generation, and visual question answering (VQA). Each of these tasks is focused on specific aspect of the CXR interpretation and uses different dataset(s).

**Image Understanding:** This category includes multi-label image classification across 14 classes using the MIMIC-CXR dataset, as well as CXR abnormality detection leveraging the VinDr-Instruct dataset. Fig. S8 shows sample input-output samples for classification and abnormality detection tasks along with the output of our model.

**Grounding:** We include four challenging grounding tasks in this work, namely: Phrase Grounding, Grounded Diagnosis, Grounded Captioning, and Anatomy Grounding. In Phrase Grounding, the model identifies the spatial location of a given phrase within an input image, utilizing the MS-CXR, PadChest-Gr, and VinDr-Instruct datasets. Grounded Diagnosis and Grounded Captioning require the model to infer a diagnosis and generate a textual description for a specified image region, respectively; we use VinDr-Instruct and MS-CXR for Grounded Diagnosis and MS-CXR for Grounded Captioning. Finally, Anatomy Grounding uses the Anatomy-Grounding dataset to localize anatomical structures based on user-provided textual prompts. Fig. 5 shows sample input and output pairs for these tasks, along with the output of our model.

**Report Generation:** This task involves generating the full report, including both the findings and impression sections using MIMIC-CXR dataset. A sample image-report is shown in Fig. S7 along with the output of Anatomix.

**Visual Question Answering:** The VQA category consists of open-ended and closed-ended question answering tasks, derived from a combination of the MIMIC-VQA, SLAKE, and Radialog-Instruct datasets.

## S5. Ablations

This section contains the detailed results for the ablations conducted for APM and  $\mathcal{LM}$ .

Table S2. Ablation results for grounding tasks. Grounded Diagnosis (GD) and Grounded Captioning (GC) results are given as: GD / GC.

Model	NLG (GD/GC)			Clinical (GD/GC)		Phrase Gr.		Anatomy Gr.	
	BERTScore	ROUGE	METEOR	RadGraph-F1	CheXbert-14-F1	IoU	mAP	IoU	mAP
AnatomiX- $I_p$	0.10 / 0.06	0.11 / 0.04	0.07 / 0.04	0.08 / 0.05	0.25 / 0.21	0.10	0.03	0.04	0.01
AnatomiX- $\hat{O}_A$	0.42 / 0.17	0.38 / 0.12	0.26 / 0.06	0.35 / 0.08	0.42 / 0.23	0.24	0.16	0.36	0.27
AnatomiX- $\hat{S}_t$	0.19 / 0.25	0.17 / 0.23	0.16 / 0.18	0.23 / 0.22	0.28 / 0.24	0.11	0.05	0.06	0.02
AnatomiX- $\hat{y}_{box}$	0.31 / 0.23	0.34 / 0.21	0.25 / 0.13	0.37 / 0.25	0.40 / 0.39	0.17	0.12	0.46	0.37
AnatomiX- $\hat{S}_t-\hat{y}_{box}$	0.49 / 0.45	0.52 / 0.36	0.34 / 0.26	0.51 / 0.34	0.49 / 0.61	0.26	0.17	0.47	0.35
AnatomiX- $\hat{O}_A-\hat{y}_{box}$	0.52 / 0.40	<u>0.58</u> / 0.33	<u>0.37</u> / 0.28	0.62 / 0.37	<u>0.50</u> / <u>0.67</u>	0.36	0.24	<u>0.61</u>	<u>0.53</u>
AnatomiX- $\hat{O}_A-\hat{S}_t$	<u>0.56</u> / <u>0.48</u>	0.54 / <u>0.45</u>	0.36 / <u>0.31</u>	<u>0.62</u> / <u>0.48</u>	<u>0.51</u> / 0.66	<u>0.42</u>	<u>0.31</u>	0.58	0.49
<b>AnatomiX</b>	<b>0.63 / 0.65</b>	<b>0.60 / 0.56</b>	<b>0.42 / 0.48</b>	<b>0.58 / 0.50</b>	<b>0.54 / 0.78</b>	<b>0.46</b>	<b>0.35</b>	<b>0.73</b>	<b>0.66</b>

Table S3. Ablations results for report generation task grouped by NLG and Clinical metrics.

Model	NLG Metrics			Clinical Metrics	
	ROUGE	BERTScore	METEOR	RadGraph	CheXbert-14 F1
AnatomiX- $I_p$	0.15	0.18	0.09	0.15	0.24
AnatomiX- $\hat{O}_A$	0.14	0.18	0.09	0.13	0.22
AnatomiX- $\hat{S}_t$	0.32	0.27	0.13	0.19	0.30
AnatomiX- $\hat{y}_{box}$	0.13	0.15	0.10	0.11	0.21
AnatomiX- $\hat{S}_t-\hat{y}_{box}$	0.27	0.24	0.10	0.15	0.23
AnatomiX- $\hat{O}_A-\hat{y}_{box}$	0.15	0.21	0.11	0.14	0.22
AnatomiX- $\hat{O}_A-\hat{S}_t$	<u>0.46</u>	<u>0.33</u>	<u>0.19</u>	<u>0.23</u>	<u>0.39</u>
<b>AnatomiX</b>	<b>0.53</b>	<b>0.38</b>	<b>0.21</b>	<b>0.26</b>	<b>0.42</b>

## S5.1. LLM

The naming convention for  $\mathcal{LM}$ 's ablations is as follows: (1) AnatomiX- $I_p$  uses only image embeddings  $I_p$ ; (2) AnatomiX- $\hat{O}_A$  augments  $I_p$  with anatomical tokens  $\hat{O}_A$ ; (3) AnatomiX- $\hat{S}_t$  combines retrieved sentences  $\hat{S}_t$  with  $I_p$ ; (4) AnatomiX- $\hat{y}_{box}$  integrates predicted bounding boxes  $\hat{y}_{box}$  with  $I_p$ ; (5) AnatomiX- $\hat{S}_t-\hat{y}_{box}$  uses  $\hat{S}_t$ ,  $\hat{y}_{box}$ , and  $I_p$ ; (6) AnatomiX- $\hat{O}_A-\hat{y}_{box}$  combines  $\hat{O}_A$ ,  $\hat{y}_{box}$ , and  $I_p$ ; and (7) AnatomiX- $\hat{O}_A-\hat{S}_t$  incorporates  $\hat{O}_A$ ,  $\hat{S}_t$ , and  $I_p$ .

Results on grounding tasks (Table S2) indicate substantial performance degradation when anatomical tokens, bounding boxes, and retrieved sentences are removed. Incorporating predicted boxes  $\hat{y}_{box}$  markedly improves anatomy grounding and further benefits other tasks when combined with  $\hat{S}_t$  and  $\hat{O}_A$ . Anatomical tokens  $\hat{O}_A$  particularly enhance phrase grounding and anatomy grounding, but contribute less to grounded captioning, which requires detailed descriptions; in this setting, retrieved sentences  $\hat{S}_t$  provide clear gains. Consistently, report generation results (Table S3) show that adding  $\hat{S}_t$  yields the largest improvement, underscoring its importance for descriptive generation. Similar patterns are observed in VQA and image understanding (Tables S4 and S5), where  $\hat{O}_A$  supports spatial reasoning, while  $\hat{S}_t$  primarily benefits linguistically intensive tasks. Overall, combining all components achieves the best performance across tasks, particularly demonstrating strong anatomical understanding.

Table S4. Performance on image classification and abnormality detection tasks.

Model	Classification	Detection	
	CheXbert-14 F1	IoU	mAP
AnatomiX- $\hat{O}_A$	0.77	0.23	0.14
AnatomiX- $\hat{S}_t$	0.81	0.11	0.05
AnatomiX- $\hat{y}_{box}$	0.78	0.18	0.10
AnatomiX- $\hat{S}_t$ - $\hat{y}_{box}$	0.83	0.21	0.13
AnatomiX- $\hat{O}_A$ - $\hat{y}_{box}$	0.79	0.28	0.19
AnatomiX- $\hat{O}_A$ - $\hat{S}_t$	0.84	0.29	0.19
AnatomiX- $I_p$	0.75	0.08	0.06
<b>AnatomiX</b>	<b>0.85</b>	<b>0.31</b>	<b>0.20</b>

Table S5. Open and close ended VQA task performance.

Model	Open-Ended VQA		Close-Ended VQA	
	BERTScore	CheXbert-14 F1	BERTScore	CheXbert-14 F1
AnatomiX- $\hat{O}_A$	0.70	0.74	0.73	0.91
AnatomiX- $\hat{S}_t$	0.81	0.84	0.81	0.94
AnatomiX- $\hat{y}_{box}$	0.67	0.72	0.76	0.90
AnatomiX- $\hat{S}_t$ - $\hat{y}_{box}$	0.78	0.79	0.83	0.95
AnatomiX- $\hat{O}_A$ - $\hat{y}_{box}$	0.73	0.75	0.79	0.85
AnatomiX- $\hat{O}_A$ - $\hat{S}_t$	0.82	0.85	0.86	<b>0.95</b>
AnatomiX- $I_p$	0.68	0.72	0.72	0.87
<b>AnatomiX</b>	<b>0.86</b>	<b>0.86</b>	<b>0.89</b>	0.95

## S5.2. APM

In addition to the ablations conducted for  $\mathcal{LM}$ , we study the contribution of different architectural components in APM. First, we replace the image encoder  $\mathcal{E}$  with a pretrained DINOv3 model, denoted as AnatomiX-Dino. Second, to evaluate the role of the feature extraction module  $\mathcal{M}$ , we remove it and perform contrastive alignment directly on the decoder output  $\mathcal{D}$ , resulting in AnatomiX-wo- $\mathcal{M}$ . Third, in APM-CLIP, we replace the proposed contrastive self-similarity loss with the standard CLIP loss. We evaluate all variants on object detection (bounding box prediction  $y_{box}$ ) and sentence retrieval. For detection, we report Intersection over Union (IoU). For retrieval, we compare the retrieved sentence  $\hat{S}_t$  with ground-truth text using CheXbert-14-F1, RadGraph-F1, and METEOR.

As shown in Table S6, DINOv3 achieves competitive IoU but underperforms on retrieval metrics, indicating weaker cross-modal alignment despite strong visual representations. Removing  $\mathcal{M}$  results in a consistent performance drop across tasks, suggesting that decoupling bounding box prediction from textual feature alignment facilitates more effective learning and improves both anatomical localization and sentence retrieval. Finally, replacing the proposed soft self-similarity loss with the standard CLIP loss degrades performance, highlighting the importance of the tailored contrastive objective in APM. Furthermore, anatomy-wise breakdown of retrieval results is given in Tables S9-S12 (d-g).

Table S6. Ablation experiments for APM discussed in S5.

Model	$y_{box}$ Metrics	$\hat{S}_t$ Metrics		
	IoU	CheXbert-14 F1	RadGraph F1	METEOR
APM-wo- $\mathcal{M}$	0.781	0.627	<u>0.689</u>	<u>0.710</u>
APM-Dino	<u>0.792</u>	0.611	0.685	0.704
APM-CLIP	0.775	<b>0.640</b>	0.679	0.692
APM	<b>0.812</b>	<u>0.634</u>	<b>0.709</b>	<b>0.727</b>

## S6. Additional Results

Table S7 contains the per dataset results for phrase grounding tasks, while Table S8 provides the per dataset breakdown for grounded diagnosis task. Furthermore, Fig. S7 shows a sample report generated using AnatomicX, and Fig. S8 shows sample input-output for VQA and image understanding tasks.

Write a comprehensive report:

---

**Generated Report**

Findings:  
The patient is status post median sternotomy and CABG. Left-sided AICD/pacemaker device is noted with leads terminating in the right atrium and right ventricle. Heart size remains mildly enlarged. Mediastinal and hilar contours are unchanged. There is mild pulmonary vascular congestion. Patchy opacities in the lung bases may reflect atelectasis. No pleural effusion or pneumothorax is present. There are no acute osseous abnormalities.

Impression:  
Mild pulmonary vascular congestion and bibasilar atelectasis.

---

**Ground Truth Report**

Findings:  
Left-sided pacer is re- demonstrated with leads terminating in the right atrium and right ventricle. The patient is status post median sternotomy, aortic valve replacement, and CABG. Heart size is mildly enlarged, unchanged. Mediastinal and hilar contours are similar. Mild upper zone pulmonary vascular redistribution is likely chronic without overt pulmonary edema. Lung volumes remain low with streaky opacities in the lung bases suggestive of atelectasis. No large pleural effusion or pneumothorax is present. Fusion hardware within the lumbar spine is partially imaged as well as hardware within the right humeral head.

Impression:  
Chronic mild pulmonary vascular congestion without overt pulmonary edema. Bibasilar atelectasis.

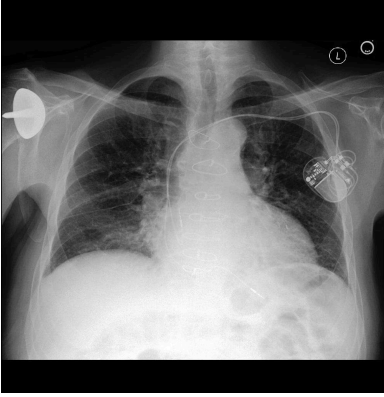


Figure S7. Sample report generation with AnatomicX.

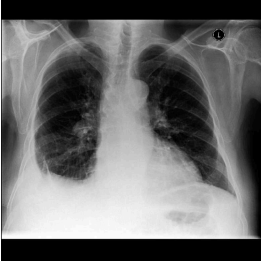
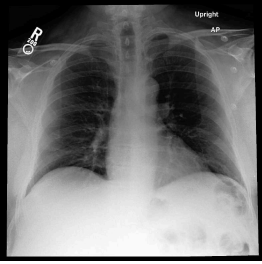
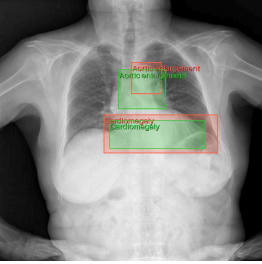

	Open-Ended VQA	Close-Ended VQA	Abnormality Detection	Classification
				
User	What are the key observations derived from this chest x-ray?	Does the image show pneumothorax?	Locate areas in the chest X-ray where abnormalities are present, using bounding box coordinates	Which diseases are represented in this image:
Model	The patient has lung opacity, atelectasis and pleural effusion.	No, there is no evidence of that in the image.	<ref>Cardiomegaly</ref><box>(399,455),(835,605)</box><ref>Aortic enlargement</ref><box>(504,252),(620,375)</box>	(X) cardiomegaly, pleural effusion, pneumonia
GT	Sure, atelectasis and pleural effusion.	No, there is not.	<ref>Cardiomegaly</ref><box>(421,478),(788,588)</box><ref>Aortic enlargement</ref><box>(454,280),(637,434)</box>	(X) cardiomegaly, pleural effusion, pneumonia

Figure S8. Example input-output-ground truth for image understanding and visual question answering tasks. Box colors: green represents the ground truth while red box shows the model's output.

Table S7. Per dataset performance on Phrase Grounding task.

Dataset	IoU	mAP
MS-CXR	0.532	0.388
PadChest-Gr	0.444	0.337
VinDr-Inst	0.230	0.180

Table S8. Grounded diagnosis performance on different datasets.

Dataset	BERTScore	ROUGE	METEOR	RadGraph-F1	CheXbert-F1
MS-CXR	0.758	0.729	0.402	0.732	0.744
VinDr-Inst	0.606	0.567	0.424	0.543	0.502

Table S9. Per-anatomy results for central anatomical structures with characteristic side predominance. (a) Results for the anatomy grounding task without flipping. (b–c) Anatomy grounding performance comparison between AnatomicX and RadVLM on flipped images. (d) Similarity between retrieved sentences  $\hat{S}_t$  and ground-truth sentences in APM.

	Heart	Aortic arch structure	Descending aorta	Superior vena cava
<b>(a) AnatomicX: Anatomy Grounding in Normal Images (no flipping)</b>				
IoU	0.60	0.73	0.76	0.75
mAP	0.71	0.63	0.64	0.65
<b>(b) AnatomicX: Anatomy Grounding in Horizontally Flipped Images</b>				
IoU	0.79	0.73	0.76	0.70
mAP	0.69	0.61	0.64	0.57
<b>(c) RadVLM: Anatomy Grounding in Horizontally Flipped Images</b>				
IoU	0.59	0.05	0.04	0.06
mAP	0.45	0.02	0.00	0.00
<b>(d) APM Sentence Retrieval Results</b>				
CheXbert-14 F1	0.92	0.41	1.00	1.00
RadGraph F1	0.63	0.57	1.00	1.00
METEOR	0.72	0.70	0.99	1.00
<b>(e) APM-wo-<math>\mathcal{M}</math> Sentence Retrieval Results</b>				
CheXbert-14 F1	0.92	0.31	1.00	1.00
RadGraph F1	0.60	0.51	1.00	1.00
METEOR	0.71	0.66	0.99	1.00
<b>(f) APM-Dino Sentence Retrieval Results</b>				
CheXbert-14 F1	0.92	0.38	1.00	1.00
RadGraph F1	0.61	0.57	1.00	1.00
METEOR	0.70	0.68	0.99	1.00
<b>(g) APM-CLIP Sentence Retrieval Results</b>				
CheXbert-14 F1	0.92	0.25	1.00	1.00
RadGraph F1	0.57	0.46	1.00	1.00
METEOR	0.67	0.64	0.99	1.00

Table S10. Anatomy-wise results for left-sided anatomical structures. (a) Results for the anatomy grounding task without flipping. (b–c) Anatomy grounding performance comparison between AnATOMiX and RadVLM on flipped images. (d) Similarity between retrieved sentences  $\hat{S}_t$  and ground-truth sentences in APM. Note: Some anatomical objects achieve a perfect score of 1.0 due to the limited number of possible sentences.

	Left lung	Left upper lung zone	Left mid lung zone	Left lower lung zone	Apical zone of left lung	Hilar area of left lung	Left costodiaphragmatic recess	Left hemidiaphragm	Left cardiophrenic sulcus	Left clavicle	Left upper abdominal quadrant	Left margin of heart
<b>(a) AnATOMiX: Anatomy Grounding in Normal Images (no flipping)</b>												
IoU	0.88	0.86	0.77	0.80	0.81	0.67	0.61	0.74	0.60	0.74	0.79	0.62
mAP	0.81	0.76	0.67	0.70	0.70	0.66	0.51	0.62	0.53	0.63	0.77	0.68
<b>(b) AnATOMiX: Anatomy Grounding in Horizontally Flipped Images</b>												
IoU	0.85	0.84	0.73	0.79	0.81	0.78	0.60	0.72	0.60	0.54	0.84	0.80
mAP	0.76	0.73	0.63	0.67	0.70	0.67	0.50	0.61	0.50	0.44	0.74	0.69
<b>(c) RadVLM: Anatomy Grounding in Horizontally Flipped Images</b>												
IoU	0.01	0.00	0.00	0.00	0.00	0.00	0.00	0.00	0.00	0.00	0.01	0.04
mAP	0.00	0.00	0.00	0.00	0.00	0.00	0.00	0.00	0.00	0.00	0.00	0.00
<b>(d) APM Sentence Retrieval Results</b>												
CheXbert-14 F1	0.58	0.11	0.15	0.31	0.32	0.39	0.34	0.85	1.00	0.75	1.00	1.00
RadGraph F1	0.49	0.49	0.45	0.55	0.70	0.57	0.71	0.76	1.00	0.64	1.00	1.00
METEOR	0.54	0.51	0.54	0.59	0.72	0.74	0.72	0.66	1.00	0.52	1.00	1.00
<b>(e) APM-wo-<math>\mathcal{M}</math> Sentence Retrieval Results</b>												
CheXbert-14 F1	0.57	0.06	0.09	0.29	0.59	0.37	0.45	0.71	1.00	0.61	1.00	1.00
RadGraph F1	0.48	0.46	0.42	0.54	0.84	0.58	0.77	0.70	1.00	0.55	1.00	1.00
METEOR	0.52	0.49	0.52	0.59	0.82	0.74	0.75	0.56	1.00	0.44	1.00	1.00
<b>(f) APM-Dino Sentence Retrieval Results</b>												
CheXbert-14 F1	0.55	0.16	0.16	0.28	0.16	0.35	0.34	0.82	1.00	0.59	1.00	1.00
RadGraph F1	0.46	0.45	0.42	0.50	0.74	0.52	0.72	0.69	1.00	0.60	1.00	1.00
METEOR	0.51	0.50	0.52	0.57	0.70	0.73	0.71	0.54	1.00	0.44	1.00	1.00
<b>(g) APM-CLIP Sentence Retrieval Results</b>												
CheXbert-14 F1	0.54	0.05	0.11	0.31	0.54	0.37	0.37	0.84	1.00	0.80	1.00	1.00
RadGraph F1	0.46	0.53	0.45	0.56	0.81	0.54	0.73	0.62	1.00	0.55	1.00	1.00
METEOR	0.50	0.50	0.51	0.58	0.80	0.73	0.72	0.46	1.00	0.46	1.00	1.00

Table S11. Anatomy-wise results for right-sided anatomical structures. (a) Results for the anatomy grounding task without flipping. (b–c) Anatomy grounding performance comparison between AnatomicX and RadVLM on flipped images. (d) Similarity between retrieved sentences  $\hat{S}_i$  and ground-truth sentences in APM. Note: Some anatomical objects achieve a perfect score of 1.0 due to the limited number of possible sentences.

	Right lung	Right upper lung zone	Right mid lung zone	Right lower lung zone	Apical zone of right lung	Hilar area of right lung	Right costodiaphragmatic recess	Right hemidiaphragm	Right cardiophrenic sulcus	Right clavicle	Right upper abdominal quadrant	Right atrial structure	Right heart border
<b>(a) AnatomicX: Anatomy Grounding in Normal Images (no flipping)</b>													
IoU	0.89	0.85	0.79	0.79	0.79	0.8	0.67	0.73	0.51	0.75	0.87	0.65	0.59
mAP	0.82	0.76	0.68	0.7	0.68	0.71	0.57	0.63	0.42	0.63	0.77	0.57	0.64
<b>(b) AnatomicX: Anatomy Grounding in Horizontally Flipped Images</b>													
IoU	0.89	0.78	0.74	0.81	0.77	0.79	0.65	0.73	0.47	0.38	0.85	0.61	0.75
mAP	0.81	0.68	0.62	0.7	0.67	0.68	0.55	0.61	0.35	0.27	0.74	0.51	0.63
<b>(c) RadVLM: Anatomy Grounding in Horizontally Flipped Images</b>													
IoU	0.0	0.0	0.0	0.0	0.0	0.0	0.0	0.01	0.0	0.0	0.01	0.0	0.0
mAP	0.0	0.0	0.0	0.0	0.0	0.0	0.0	0.0	0.0	0.0	0.0	0.0	0.0
<b>(d) APM Sentence Retrieval Results</b>													
CheXbert-14 F1	0.6	0.05	0.1	0.25	0.5	0.4	0.4	0.8	1.0	0.73	1.0	1.0	1.0
RadGraph F1	0.5	0.44	0.43	0.49	0.76	0.54	0.76	0.73	1.0	0.62	1.0	1.0	1.0
METEOR	0.55	0.5	0.53	0.57	0.75	0.74	0.74	0.61	1.0	0.49	1.0	1.0	1.0
<b>(e) APM-wo-<math>\mathcal{M}</math> Sentence Retrieval Results</b>													
CheXbert-14 F1	0.57	0.03	0.09	0.28	0.48	0.39	0.49	0.6	1.0	0.7	1.0	1.0	1.0
RadGraph F1	0.48	0.41	0.39	0.52	0.64	0.55	0.78	0.62	1.0	0.59	1.0	1.0	1.0
METEOR	0.53	0.48	0.52	0.58	0.74	0.74	0.76	0.47	1.0	0.43	1.0	1.0	1.0
<b>(f) APM-Dino Sentence Retrieval Results</b>													
CheXbert-14 F1	0.57	0.05	0.1	0.24	0.35	0.38	0.41	0.63	1.0	0.78	1.0	1.0	1.0
RadGraph F1	0.47	0.47	0.37	0.47	0.74	0.51	0.73	0.61	1.0	0.61	1.0	1.0	1.0
METEOR	0.53	0.5	0.51	0.56	0.72	0.72	0.72	0.43	1.0	0.5	1.0	1.0	1.0
<b>(g) APM-CLIP Sentence Retrieval Results</b>													
CheXbert-14 F1	0.56	0.05	0.09	0.24	0.7	0.4	0.53	0.85	1.0	0.91	1.0	1.0	1.0
RadGraph F1	0.47	0.48	0.4	0.51	0.81	0.53	0.76	0.69	1.0	0.56	1.0	1.0	1.0
METEOR	0.53	0.5	0.51	0.57	0.79	0.73	0.75	0.57	1.0	0.45	1.0	1.0	1.0

Table S12. Anatomy-wise results for midline (central) anatomical structures. (a) Results for the anatomy grounding task without flipping. (b–c) Anatomy grounding performance comparison between AnatoMiX and RadVLM on flipped images. (d) Similarity between retrieved sentences  $\hat{S}_i$  and ground-truth sentences in APM.

	Trachea & main bronchus	Carina	Mediastinum	Superior mediastinum	Vertebral column	Cavoatrial	Abdominal cavity
<b>(a) AnatoMiX: Anatomy Grounding in Normal Images (no flipping)</b>							
IoU	0.74	0.48	0.58	0.77	0.85	0.66	0.86
mAP	0.62	0.40	0.73	0.67	0.74	0.57	0.81
<b>(b) AnatoMiX: Anatomy Grounding in Horizontally Flipped Images</b>							
IoU	0.75	0.47	0.70	0.77	0.76	0.38	0.84
mAP	0.64	0.35	0.59	0.66	0.65	0.29	0.77
<b>(c) RadVLM: Anatomy Grounding in Horizontally Flipped Images</b>							
IoU	0.43	0.05	0.60	0.68	0.74	0.00	0.81
mAP	0.31	0.01	0.47	0.56	0.62	0.00	0.67
<b>(d) APM Sentence Retrieval Results</b>							
CheXbert-14 F1	1.00	0.83	0.44	0.06	0.65	0.99	0.89
RadGraph F1	1.00	0.80	0.47	0.29	0.68	0.64	0.81
METEOR	0.99	0.86	0.45	0.44	0.62	0.57	0.82
<b>(e) APM-wo-<math>\mathcal{M}</math> Sentence Retrieval Results</b>							
CheXbert-14 F1	1.00	0.91	0.43	0.09	0.69	0.99	0.88
RadGraph F1	1.00	0.87	0.43	0.18	0.60	0.47	0.80
METEOR	0.99	0.91	0.43	0.45	0.61	0.32	0.83
<b>(f) APM-Dino Sentence Retrieval Results</b>							
CheXbert-14 F1	1.00	0.89	0.40	0.05	0.57	0.99	0.88
RadGraph F1	1.00	0.88	0.44	0.21	0.55	0.50	0.82
METEOR	0.99	0.92	0.42	0.39	0.59	0.45	0.82
<b>(g) APM-CLIP Sentence Retrieval Results</b>							
CheXbert-14 F1	1.00	0.79	0.44	0.02	0.59	0.99	0.78
RadGraph F1	1.00	0.75	0.37	0.22	0.64	0.44	0.58
METEOR	0.99	0.82	0.37	0.43	0.55	0.22	0.59

## S7. Attention Visualization

In this section, we visualize the cross-attention weights learned within the feature extraction module  $\mathcal{M}$  using the anatomical object tokens  $O_A$  as queries and image patch embeddings  $I_p$  as keys. Fig. S9 shows that the model focuses on the correct region in the image with high accuracy leading to rich anatomical object tokens  $\hat{O}_A$  and overall anatomical understanding in the downstream tasks.

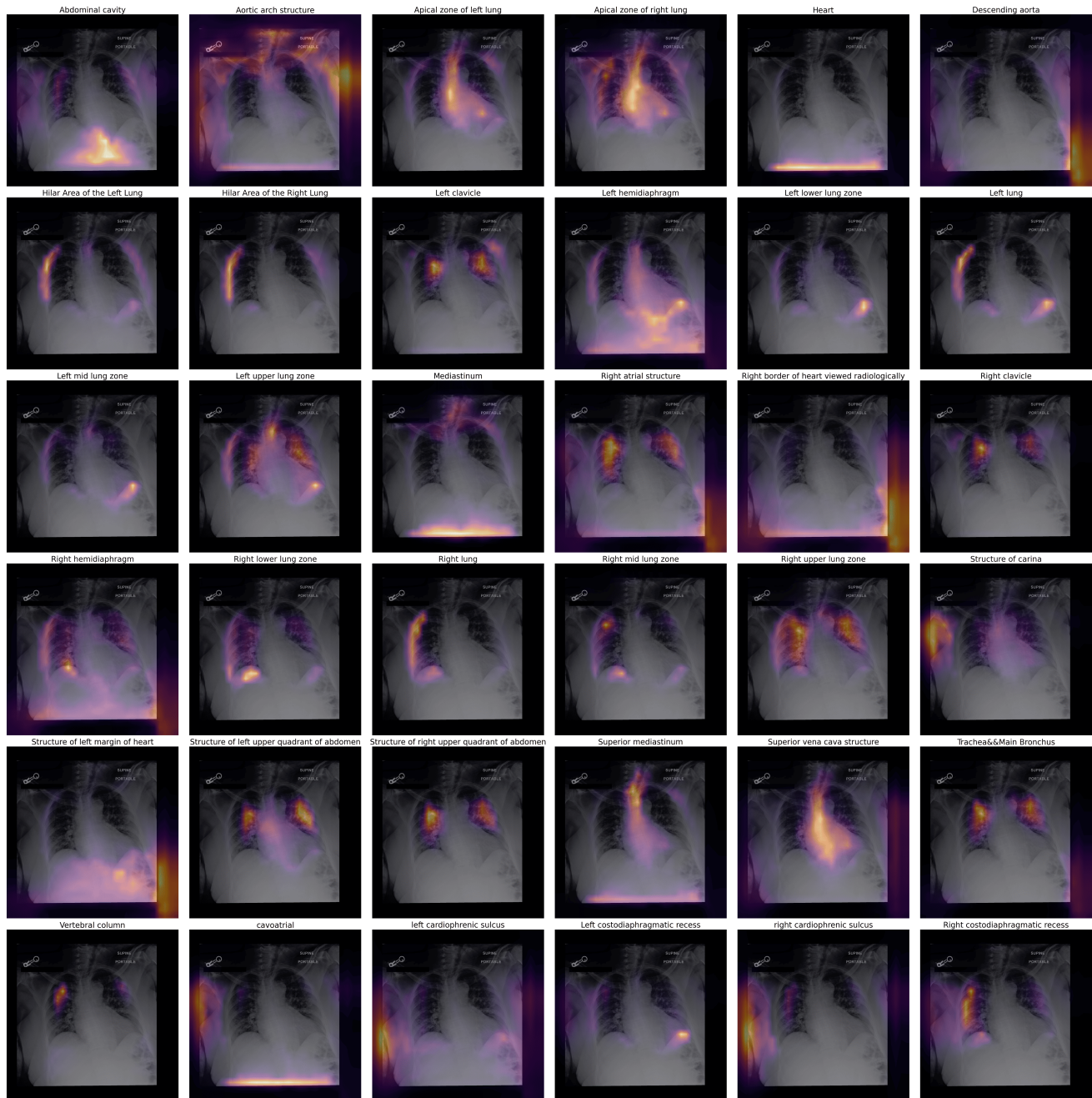


Figure S9. Cross-attention between anatomical object tokens and image embeddings in the feature extraction module  $\mathcal{M}$ . Subfigure titles indicate the corresponding anatomical object names. Best viewed when zoomed in.